



Laser-Raman Measurements in a Ducted, Two-Stream, Subsonic H₂/Air Combustion Flow

W. D. Williams, H. M. Powell,
L. L. Price, and G. D. Smith
ARO, Inc.

December 1979

Final Report for Period September 5, 1978 – August 13, 1979

Approved for public release; distribution unlimited.

**ARNOLD ENGINEERING DEVELOPMENT CENTER
ARNOLD AIR FORCE STATION, TENNESSEE
AIR FORCE SYSTEMS COMMAND
UNITED STATES AIR FORCE**

NOTICES

When U. S. Government drawings, specifications, or other data are used for any purpose other than a definitely related Government procurement operation, the Government thereby incurs no responsibility nor any obligation whatsoever, and the fact that the Government may have formulated, furnished, or in any way supplied the said drawings, specifications, or other data, is not to be regarded by implication or otherwise, or in any manner licensing the holder or any other person or corporation, or conveying any rights or permission to manufacture, use, or sell any patented invention that may in any way be related thereto.

Qualified users may obtain copies of this report from the Defense Documentation Center.

References to named commercial products in this report are not to be considered in any sense as an endorsement of the product by the United States Air Force or the Government.

This report has been reviewed by the Information Office (OI) and is releasable to the National Technical Information Service (NTIS). At NTIS, it will be available to the general public, including foreign nations.

APPROVAL STATEMENT

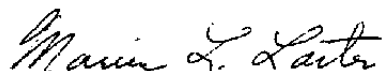
This report has been reviewed and approved.



ELTON R. THOMPSON
Project Manager
Directorate of Technology

Approved for publication:

FOR THE COMMANDER



MARION L. LASTER
Director of Technology
Deputy for Operations

UNCLASSIFIED

UNCLASSIFIED

20. ABSTRACT (Continued)

investigated. The radial distributions of static temperature and species number densities were determined at several axial positions for each test condition.

UNCLASSIFIED

PREFACE

The work reported herein was conducted by the Arnold Engineering Development Center (AEDC), Air Force Systems Command (AFSC) for the Directorate of Technology. The results of the experiments were obtained by ARO, Inc., AEDC Division (a Sverdrup Corporation Company), operating contractor for the AEDC, AFSC, Arnold Air Force Station, Tennessee, under ARO Project Numbers V32I-P1A, E32P-POA, and P32M-01. The Air Force project managers were Capt. Stanislaus L. Ludwig (CF) and Mr. Elton R. Thompson. The data analysis was completed on August 13, 1979, and the manuscript was submitted for publication on September 20, 1979.

CONTENTS

	<u>Page</u>
1.0 INTRODUCTION	
1.1 Purpose of the Experiments	7
1.2 Objectives	7
1.3 Description of the Flow Field	7
2.0 EXPERIMENTAL SETUP AND OPERATION	
2.1 Test Cell	8
2.2 Laser System	8
2.3 Spectrometer System	9
2.4 Data Acquisition System	9
3.0 LASER-RAMAN MEASUREMENT TECHNIQUE	
3.1 Spectra and Intensity Relations	10
3.2 Calibrations	12
3.3 Data Reduction	13
4.0 DISCUSSION	
4.1 Presentation of Data	16
4.2 Data Uncertainty	16
4.3 Comparison of Results for the Two Test Cases	18
4.4 Comparison of the Results with Calculations	19
5.0 SUMMARY	19
REFERENCES	21

ILLUSTRATIONS

Figure

1. Turbulent, Ducted, Mixing System with Recirculation	23
2. Recirculating-Flow-Combustor Simulation Facility	24
3. Laser-Raman Experimental Configuration at AEDC-ETF Research Cell R1A-1	25
4. Block Diagram of Electronic Systems Applicable During the Data Acquisition Interval, Q-Switch/Integrator Technique	26
5. Typical Timing Diagram for Data Acquisition Sequence	28
6. Pure Rotational Raman Spectrum, N_2 and O_2 at $T = 300$ K; $[N_2]/[O_2] = 3.73$	29
7. Pure Rotational Raman Spectrum, N_2 and O_2 at $T = 900$ K; $[N_2]/[O_2] = 3.73$	30

<u>Figure</u>	<u>Page</u>
8. Pure Rotational Raman Spectrum, N_2 and O_2 at $T = 1500$ K; $[N_2]/[O_2] = 3.73$	31
9. Pure Rotational Raman Spectrum, N_2 and H_2 at $T = 300$ K; $[N_2]/[H_2] = 0.667$	32
10. Pure Rotational Raman Spectrum, N_2 and H_2 at $T = 900$ K; $[N_2]/[H_2] = 0.667$	33
11. Pure Rotational Raman Spectrum, N_2 and H_2 at $T = 1500$ K; $[N_2]/[H_2] = 0.667$	34
12. Intensity Ratio, I_c (7061 Å)/ I_c (7010 Å), as a Function of Temperature	35
13. Intensity Ratio, I_c ($J = 1, H_2$)/ I_c ($J = 2, H_2$), as a Function of Temperature	36
14. $J = 1, H_2$ Line Intensity Relative Temperature Dependence	37
15. I_c (7010 Å) Relative Temperature Dependence	38
16. N_2 Vibration-Rotation Band, Q-Branch Intensity Relative Temperature Dependence	39
17. Isometric Plot of Measured Radial Temperature Distribution, DTINDR = 2; 0.55-, 5.25-, and 10.5-in. Axial Positions	40
18. Isometric Plot of Measured Radial Temperature Distribution, DTINDR = 2; 15.75-, 21-, 26.25-, and 31.5-in. Axial Positions	41
19. Isometric Plot of Measured Radial Temperature Distribution, DTINDR = 10; 2.5-, 5.25-, and 10.5-in. Axial Positions	42
20. Isometric Plot of Measured Radial Temperature Distribution, DTINDR = 10; 15.75-, 21-, and 26.25-in. Axial Positions	43
21. Air Number Density as a Function of Flow-Field Position, DTINDR = 2	44
22. Number Density as a Function of Flow-Field Position, DTINDR = 2	45
23. Number Density as a Function of Flow-Field Position, DTINDR = 10	46
24. Axial Centerline Variation of $n(\text{air})$ for Both Test Configurations	47
25. Axial Variation of $n(\text{air})$ for Both Test Configurations	48
26. Instantaneous Temperatures versus Laser Pulse Number	49
27. Instantaneous Temperatures versus Laser Pulse Number	50
28. Systematic Fractional Error in Temperature and Number Density Measurements as a Function of Temperature	51

Page**TABLES**

1. Measured Values of Temperature and Number Density and Estimated Uncertainty, DTINDR = 2	52
2. Measured Values of Temperature and Number Density and Estimated Uncertainty, DTINDR = 10	55
NOMENCLATURE	59

1.0 INTRODUCTION

1.1 PURPOSE OF THE EXPERIMENTS

A common feature of many combustion flow fields is the recirculation zone established by turbulent mixing in a constant-area, axisymmetric duct of two coaxial flows (Ref. 1). An example relevant to aerospace applications is the so-called "sudden" expansion or "dump" combustors used in ramjet-rocket propulsion systems that are designed on the principle of establishing and maintaining combustion in regions of recirculating flow within the combustor. Analytical techniques must be developed and evaluated for analyzing and predicting the turbulent mixing and combustion phenomena for various configurations. However, there is a lack of experimental flow-field information for such configurations. Therefore, the primary purpose of these experiments was to obtain data to aid the development of ducted, recirculating flow models. In addition, the laser-Raman diagnostic technique was to be used to obtain the data to demonstrate the utility of the technique in hostile, AEDC test cell environments.

1.2 OBJECTIVES

The primary objective was to use laser-Raman scattering to provide a flow-field map of rotational temperature for two combustor configurations. Because of the high gas density (near atmospheric) in the flow field, the static (or translational) and rotational temperatures are essentially equal. The use of a pulsed laser with a nominal pulse width of 25 nsec made the measurements essentially instantaneous. Therefore, a precise average temperature could be obtained by accumulating a large number of these instantaneous measurements at each flow-field position. A second objective was to map species number density for the two configurations.

1.3 DESCRIPTION OF THE FLOW FIELD

Figure 1, reproduced from Ref. 1, shows the essential features of the flow field. For these experiments, the higher-velocity, primary jet stream was air, and the lower-velocity, secondary stream was hydrogen. Whenever the entrainment, or pumping capacity, of the primary jet is greater than the mass flow of the secondary stream, the eddy of the recirculation region is generated (Fig. 1). The recirculation eddy provides mass flux to balance the jet entrainment requirements. Although the recirculation eddy can exist with or without secondary flow, the recirculation eddy structure disappears if the secondary mass flow rate is increased to some critical value. The duct flow will then be characterized by positive axial velocities throughout.

2.0 EXPERIMENTAL SETUP AND OPERATION

2.1 TEST CELL

The experiments were conducted in the AEDC Engine Test Facility Propulsion Research Cell (R1A-1), detailed in Refs. 1 and 2 and shown as modified for these experiments in Fig. 2. The 0.6-cm (1/4-in.)-wide slot permitted viewing of the laser beam focal volume over the full width of the flow field. Observations were made through a 22.9-cm (9-in.)-diam quartz window. Entrance and exit ports were added to the top and bottom of the slot to permit the high-energy laser beam to be focused within the flow field. These ports were also made of quartz.

The test chamber was a 3.5-m (5-ft)-long stainless-steel duct with an inside diameter of 13.3 cm (5.24-in.). A mechanically driven, axially traversing nozzle assembly was mounted inside the duct, and an O-ring system provided the seal between the assembly and the duct. The nozzle assembly included either a 1.33-cm (0.524-in.)- or a 6.65-cm (2.62-in.)-diam nozzle that produced the primary air jet and an annular assembly that injected hydrogen into the duct, the walls of which were cooled by an external water spray. To stabilize the flow, the secondary hydrogen flow passed through two porous plates and a screen pack. A spark plug was located downstream of the observation point to ignite the combustible hydrogen-air mixture.

2.2 LASER SYSTEM

The laser system was mounted on the top tier of an aluminum table and directly above the spectrometer system, which was mounted on the lower part of the table (see Fig. 3). The aluminum table was securely clamped to a hydraulically operated traversing table that was used to move the entire system vertically and horizontally.

The laser was a Holobeam 600 series pulsed ruby operated in the Q-switch mode. The ruby rod was 15.2-cm (6 in.) in length and 1.2 cm (0.5-in.) in diameter. A Pockels cell provided the Q-switching mechanism; the pulse repetition rate was 15 per minute.

The output beam from the laser was expanded in the ratio 3:1 and focused with a 1000-mm-focal-length, fused silica lens at a point inside the test chamber. After the laser beam passed through the chamber, a lens reduced the size of the beam diameter to permit detection of the beam energy by a pyroelectric detector. Appropriate beam attenuators were installed at the entrance to the pyroelectric detector to prevent damage.

A second type of laser energy monitor was installed at the rear of the Pockels cell. A portion of the very weak beam transmitted by the rear mirror of the Pockels cell was

split off, passed through laser line filters, and detected by a photomultiplier tube. The output of the photomultiplier could be either displayed on a storage scope for inspection of laser pulse shape or integrated to give a measure of the laser output energy.

To facilitate alignment of the ruby laser system, a helium-neon (He-Ne) laser was installed behind the rear laser energy monitor. The He-Ne laser was initially aligned through the center of all the ruby laser optics to keep the center of the ruby beam coincident with that of the He-Ne beam. Any necessary adjustments or periodic checks on system alignment could be accomplished by using the He-Ne beam.

2.3 SPECTROMETER SYSTEM

Two 25.4-cm (10-in.)-focal-length quartz lenses were used to collect the laser scattered radiation and to image the observation volume with unit magnification onto the 2-mm-wide entrance slit of the spectrometer. An aperture at the entrance slit selected a 0.3-cm (1/8-in.) beam length for observation.

The spectrometer was an 0.85-m-focal-length double spectrometer with 1200 g/mm gratings. The regular single-exit-slit assembly was removed and replaced with a 2-mm-wide, double-slit assembly. Exit slit radiation was coupled to dual detectors by means of adjustable mirrors and lenses. The detectors were cooled (-26°C) RCA® C31034A photomultiplier tubes (PMT).

2.4 DATA ACQUISITION SYSTEM

The technique used for this application integrated over time the PMT output current for an interval no less than that of the pulse duration. For background radiation subtraction, a similar integration was performed without laser excitation. Because of the very short pulse duration, extremely fast integration was required. The LeCroy Model 2250L integrator was found to be adequate for this application. Each channel had a common gate control and individual analog-to-digital (A/D) converters. The converter outputs were stored in a 32-deep, first-in-first-out (FIFO) memory; consequently, up to 16 laser shots were possible for a single run series. These results were averaged and printed out as individual laser shots and averaged for the run. The pyroelectric detection system was also read by the processor and similarly averaged.

The block diagram of the system is shown in Fig. 4. The corresponding timing diagram is shown in Fig. 5. The data interval sequence began upon generation of the Q-switch trigger pulse which occurred after the flash lamp excitation. This pulse occurred 610 μ sec after the flash lamp excitation, which corresponded to optimum laser performance, and approximately 250 μ sec before the energy pulse. The charging of the

laser capacitor was controlled from the processor and was repeated a preselected number of times. The processor counted the interval flags and compared the count to a preset number in memory. The laser was in a free-running mode and fired automatically. The FIFO memory was read out to the processor at the end of each series. The Q-switch synchronization (sync) pulse triggered a storage oscilloscope that was used to monitor the timing features of the data acquisition functions. The oscilloscope gate pulse, in turn, triggered the gate pulse generator. System delays and an adjustable delay in the pulse generator accounted for the 250-nsec separation between the sync pulse and the Q-switch energy pulse and for any additional delay differentials in the interconnecting coaxial lines. The adjustable delays were selected to insure coincidence of the data gate and the detector signals at the integrators. Differentials in lengths of cable and light paths between the laser energy monitor and PMT signals were accounted for by adjustments in coaxial line length. These adjustments were made by applying appropriate signals to the storage oscilloscope and adjusting the delay on the gate generator while making repeated laser firings.

The oscilloscope gate was used to trigger a one-shot, multivibrator control pulse (Figs. 4 and 5). The data interval pulse (OS/1) is a flag used by the computer to indicate that data input to the integrator has been started and completed. Background data were obtained by the double-pulse mode selection on the gate pulse generator. Pulse separation was adjusted to 12 μ sec. Since 9 μ sec are required for conversion and 1 μ sec for transfer to FIFO memory, the overall effect was to follow the laser scattering data with a background measurement of the same integration interval. After $N = 16$ background pulse and data combinations, the sequence was shut down. The data interval (OS/1) flagged the processor either to reset the laser charge condition or to terminate the run, read the data from the FIFO memory of the integrator module, converted the results to decimal, and printed the results.

3.0 LASER-RAMAN MEASUREMENT TECHNIQUE

3.1 SPECTRA AND INTENSITY RELATIONS

As a result of inelastic collisions between laser beam photons and gas molecules, laser radiation is scattered from the beam at frequencies other than that of the laser. This phenomenon, known as Raman scattering, is detailed in Refs. 3 through 6. Radiation scattered at longer wavelengths (lower frequencies) is commonly referred to as Stokes Raman scattering; only the Stokes wavelengths were used in these experiments. If the inelastic collisions between the laser photons and gas molecules cause only rotational energy level changes in the molecules, pure rotational Raman scattering results and the spectra will be observed in the $\leq 1000\text{-cm}^{-1}$ region from the laser wavelength. For the

flow field under study, the gas species expected in the spectra were N_2 , O_2 , H_2 , and H_2O . With the Raman Spectral Program (RASP)* variation of the relative intensity of the spectral lines of N_2 , O_2 , and H_2 with temperature can be readily calculated. Figures 6 through 8 are calculations of the Stokes rotational Raman spectra of N_2 and O_2 in air, and the spectra have been convolved with the transmission function of the spectrometer used in these experiments. The variation of the spectral profile with temperature can be observed clearly in Figs. 6 through 8. Similar calculations for a mixture of N_2 and H_2 ($[N_2]/[H_2] = 0.667$) are shown in Figs. 9 through 11. The temperature-dependent intensity ratio $R(T_R)$ for the spectral locations 7010 Å and 7061.2 Å defined by

$$R(T_R) = \frac{I_c(7061.2 \text{ } \text{\AA})}{I_c(7010 \text{ } \text{\AA})} \quad (1)$$

has been computed using RASP and is shown in Fig. 12 for both air and pure N_2 for $300 \text{ K} \leq T_R \leq 3000 \text{ K}$. For the flow field under study, the actual ratio must lie somewhere between these two calculated extremes. It has been assumed that the weak and widely dispersed pure rotational spectrum of H_2O can be neglected; the spectral measurements of Ref. 7 justify this assumption. The intensity ratios of the $J=1$ (7238 Å) and $J=2$ (7359 Å) H_2 lines have also been calculated and are shown in Fig. 13. By using the measured values of the intensity ratios and the predicted curves of Figs. 12 and 13, temperature values can be determined from both the N_2/O_2 - and the H_2 -rotational Raman scattering profiles.

The intensities of the Raman lines of the molecules are directly proportional to the number densities of the molecular species. The intensity of the $J=1$ (7238 Å), H_2 rotational line can be expressed as

$$I_m(J=1, H_2) = n(H_2) \left[C_F(H_2) C_{F_3}(T) \right]^{-1} \quad (2)$$

in which $n(H_2)$ is the hydrogen number density, $C_F(H_2)$ is a proportionality factor, and $C_{F_3}(T)$ is a temperature-dependent term. A RASP calculation of $C_{F_3}(T)$ is given in Fig. 14. If it is assumed that temperature has been measured and that $C_F(H_2)$ has been determined by calibration, then $n(H_2)$ can be determined from

$$n(H_2) = C_F(N_2) C_{F_3}(T) I_m^t(J=1, H_2) \quad (3)$$

* Developed at AEDC by W. D. Williams, et al.

Similarly, the number density of air, $n(\text{air})$, and N_2 , $n(\text{N}_2)$, can be determined, respectively, from the following relations:

$$n(\text{air}) = C_F(\text{air}) C_{F_1}(T) I_m^t (7010 \text{ \AA}), \quad (4)$$

$$n(\text{N}_2) = C_F(\text{N}_2) C_{F_2}(T) I_m^t (7010 \text{ \AA}) \quad (5)$$

The results of the RASP calculations of $C_{F_1}(T)$ and $C_{F_2}(T)$ are graphed in Fig. 15.

Since the inelastic collisions between laser beam photons and molecules result in vibrational level transitions, the Raman vibration-rotation bands, which are displaced in magnitude from the laser source wave number by $\gtrsim 1000 \text{ cm}^{-1}$, can be observed. Unlike pure rotational structures, these bands provide a high degree of molecular specificity. Since the intensity of each band is directly proportional to the molecular species number density, the intensity of the N_2 vibration-rotation band Q-branch at 8283 \AA can be expressed as

$$I_m(\text{N}_2, Q) = n(\text{N}_2) [C_F(\text{N}_2, Q) C_{F_4}(T)]^{-1} \quad (6)$$

Again, if temperature has been measured and if the rotational and vibrational modes are in equilibrium, then the N_2 number density can be determined with Eq. (6). The plot of $C_{F_4}(T)$ as a function of temperature is given in Fig. 16.

3.2 CALIBRATIONS

Calibrations were conducted before each test period. A slow, steady flow of either pure N_2 or air maintained atmospheric pressure in the test cell. These calibrations were used to determine $C_F(\text{N}_2)$ and $C_F(\text{air})$. The relative sensitivity of the detectors at 7010 \AA (C_{F_R}) was also determined.

Because of the need to perform radial surveys of the flow field, it was also necessary to calibrate the optical sensitivity of the system as a function of the radial position of the laser focal volume. With a flow of either pure N_2 or air, the Raman signal at 7010 \AA was measured over the lower half of the flow field at 0.3-cm ($1/8\text{-in.}$) intervals. Only minor changes in relative sensitivity were noted until within 0.6 cm ($1/4 \text{ in.}$) of the cell wall, at which point collection solid angle began to be rapidly decreased. Therefore, no test measurements were made closer to the wall than 0.6 cm .

3.3 DATA REDUCTION

Nominally fifteen laser pulses were used for each measurement point within the flow field. For each laser pulse an intensity ratio, R_i , was determined with the relation

$$R_i = \frac{I_{mi}(7061.2 \text{ \AA}) C_{FR}}{I_{mi}(7010 \text{ \AA})} \quad (7)$$

and a corresponding temperature, T_i , was then determined by graph. The ensemble average of these temperature values provided an initial value of average temperature at the measurement point using

$$\overline{T_R(R)} = \sum_{i=1}^k \frac{T_i}{k} \quad (8)$$

where k is the number of laser pulses per data point. The fractional rms deviation of the initial average temperature was determined from

$$S_{\overline{T}} = \frac{\left[\sum_{i=1}^k (\delta T_i)^2 \right]^{1/2}}{k \overline{T_R(R)}} \quad (9)$$

in which

$$\delta T_i = T_i - \overline{T_R(R)}$$

Because of the nonlinearity of the R versus T curves and the limited number of laser pulses per data point, an additional correction procedure must be adopted to arrive at a true average temperature value, \overline{T}_R (Refs. 8 and 9). The true average temperature can be estimated as

$$\overline{T}_R = \overline{T_R(R)} - \epsilon_M \quad (10)$$

in which

$$\epsilon_M = \frac{1}{2} \left(\frac{d^2 T}{d R^2} \right)_{R_o} R_o^2 \left[\frac{1}{(M'_{ai})^2} + \frac{1}{(M'_{bi})^2} + \frac{(M'_{ai})^2}{(M'_{ai})^2 + (M'_{bi})^2} \right] \quad (11)$$

The M'_i values are fluctuation measures defined as follows:

$$M_i = 1 + M'_i \quad (12)$$

in which M_i is a factor to account for detector shot noise and turbulent medium fluctuations. M_i is a random number which is Poisson distributed about unity; i.e.,

$$\bar{M}_i = 1, \bar{M}'_i = 0 \quad (13)$$

To evaluate ϵ_M it must be noted that the shot noise and turbulent medium fluctuations are uncorrelated, a condition that allows the neglect of the product term of M_i values. Further,

$$S_R^2 = \overline{(M'_{ai})^2} + \overline{(M'_{bi})^2} \quad (14)$$

in which S_R is the fractional rms fluctuation of the measured intensity ratio value. S_R is calculated from the following equation:

$$S_R = \frac{\left[\sum_{i=1}^k \frac{(\delta R_i)^2}{R} \right]^{1/2}}{R} \quad (15)$$

in which

$$\bar{R} = \sum_{i=1}^k \frac{R_i}{k}$$

and

$$\delta R_i = R_i - \bar{R}$$

The value of R corresponding to $\overline{T_R(R)}$ is defined to be R_0 . For $300 \leq \overline{T_R(R)} < 1200$ K,

$$\frac{d^2 T}{d R^2} = -0.825554 \times 10^5 + (1.362582 \times 10^6) R \quad (16)$$

$$-(7.289328 \times 10^6) R^2 + (12.50538 \times 10^6) R^3$$

For $1200 \leq \bar{T}_R(R) \leq 3000$ K,

$$\begin{aligned} \frac{d^2 T}{d R^2} = & 1.152546 \times 10^3 - (0.610152 \times 10^4) R \\ & + (3.473112 \times 10^4) R^2 - (2.20656 \times 10^4) R^3 \end{aligned} \quad (17)$$

The second-order derivatives were obtained from a fifth-order polynomial fit to the T_R versus R curve in Fig. 12.

Initial air number densities were obtained from

$$\overline{n(\text{air})}^{(1)} = C_F(\text{air}) C_{F_1}(\bar{T}_R) \overline{I_m^1(7010 \text{ \AA})} \quad (18)$$

However, as can be seen in Fig. 15, $C_{F_1}(T)$ is not a linear function of temperature. Therefore, a correction is required to obtain the true number density values:

$$\overline{n(\text{air})} = \overline{n(\text{air})}^{(1)} - \epsilon_n \quad (19)$$

in which

$$\epsilon_n = \frac{1}{2} \left[\frac{d^2 C_{F_1}}{dT^2} \right]_{\bar{T}_R} \hat{S}_T^2 C_F(\text{air}) \overline{I_m^1(7010 \text{ \AA})} \quad (20)$$

and

$$\hat{S}_T = S_{\bar{T}}(k)^{1/2} \quad (21)$$

A radial profile of H_2 number density was obtained at one axial position. However, because of a lack of test time for obtaining a calibration in H_2 , the density values had to be presented as only relative density values. At the same axial position a radial profile of N_2 number density was obtained by using the N_2 vibration-rotation band and the following relation

$$\overline{n(N_2)} = C_F(N_2, Q) C_{F_4}(\bar{T}_R) \overline{I_m(N_2, Q)} \quad (22)$$

No correction was applied because of the near-linear dependence of C_{F_4} on temperature over the range of temperatures and temperature fluctuations encountered.

4.0 DISCUSSION

4.1 PRESENTATION OF DATA

Tabulations of the laser-Raman results are given in Tables 1 and 2. Figures 17 through 23 show the radial variations of the temperature and number density values; Figs. 24 and 25 show the axial variations of number density.

Average minimum temperatures are approximately 320 K, and average maximum to temperatures are approximately 1500 K. It was anticipated that maximum temperatures near 2500 to 3000 K would be observed in the combustion regions of the flow, and instantaneous values of temperature were observed to be this high (Figs. 26 and 27). It is speculated that the high-temperature combustion zones may have had a spatial extent smaller than the cylindrical Raman observation volume of approximately 1-mm diam and 3.18-mm length.

Number density values were obtained predominantly from the intensity measurements of the rotational structure. The N_2/O_2 mole fraction ratio was unknown a priori; therefore, number density values were reduced in accordance with the assumption of an N_2/O_2 mole fraction ratio of 3.73 (i.e., air). This assumption results in a large uncertainty (discussed in Section 4.2) for the combustion zones in which the O_2 concentration is depleted. However, for regions at or near the axial centerline and near the nozzle exit plane, the assumption is valid, and it should be noted that, as expected, the number densities are near atmospheric values.

4.2 DATA UNCERTAINTY

Data uncertainty values are given for each data point in Tables 1 and 2. These were calculated with the relation

$$U = B \pm S \quad (23)$$

in which B represents the fractional systematic error and S represents the fractional random error. Equation (23) gives a range of uncertainty (minimum, maximum) for the measurements. For the temperature measurements, the uncertainty was calculated with

$$U_T = B_T \pm S_{\bar{T}} \quad (24)$$

The $S_{\bar{T}}$ values are also given for each data point in Tables 1 and 2. The systematic error (or bias) results from the assumption that the N_2/O_2 mole fraction was 3.73 (i.e., the same as for air). As shown in Fig. 12, the maximum uncertainty would result if the O_2 were completely depleted and if the R versus T_R curve for N_2 had been used. By using the results shown in Fig. 12, the maximum systematic error was calculated as a function of temperature and is plotted in Fig. 8. From this plot, the values of B_T were determined.

The uncertainty for the density measurements was calculated using

$$U_n = -B_n \pm S_{\bar{T}} \quad (25)$$

The systematic error results from the N_2/O_2 mole fraction assumption. As shown in Fig. 15, the maximum uncertainty would result if the O_2 were completely depleted and if the $C_{F_2}(T_2)$ versus T_R curve had been used. The maximum systematic error calculated with the use of Fig. 15 is plotted as a function of temperature in Fig. 28. From this plot the values of B_n were determined.

The random error of the density measurements was calculated as follows:

$S_n' \equiv$ the fractional rms deviation of the intensity measurement

$$S_n' = \frac{\left[\sum_{i=1}^k \left(\frac{\delta I_{m,i}^t (7010 \text{ \AA})}{I_m^t (7,010 \text{ \AA})} \right)^2 \right]^{1/2}}{(k) I_m^t (7,010 \text{ \AA})} \quad (26)$$

$S_n'' \equiv$ the fractional deviation of the $C_{F_1}(\bar{T}_R)$ value resulting from the imprecision of the temperature measurement

$$S_n'' = S_{\bar{T}} \bar{T}_R \left(\frac{dC_{F_1}(T)}{dT} \right)_{\bar{T}_R} \quad (27)$$

For $300 \text{ K} \leq \bar{T}_R < 1200 \text{ K}$,

$$\begin{aligned} \frac{dC_{F_1}(T)}{dT} = & -2.803029225 \times 10^{-2} + (1.357945891 \times 10^{-4}) T \\ & - (2.468528696 \times 10^{-7}) T^2 + (1.975217603 \times 10^{-10}) T^3 \\ & - (5.840266985 \times 10^{-14}) T^4 \end{aligned} \quad (28)$$

For $1200 \text{ K} \leq \bar{T}_R \leq 3000 \text{ K}$,

$$\begin{aligned} \frac{dC_{F1}(T)}{dT} = & 7.849181548 \times 10^{-4} - (1.61032032 \times 10^{-6}) T \\ & + (1.218008693 \times 10^{-9}) T^2 - (3.981211523 \times 10^{-13}) T^3 \\ & + (4.783911592 \times 10^{-17}) T^4 \end{aligned} \quad (29)$$

$S_{\bar{n}}$ \equiv the random error of the density measurements as follows:

$$S_{\bar{n}} = \left[(S_{\bar{n}}')^2 + (S_{\bar{n}}'')^2 \right]^{1/2} \quad (30)$$

4.3 COMPARISON OF RESULTS FOR THE TWO TEST CASES

The contrast between the flow fields of the two test configurations is striking. For DTINDR = 2, the fuel-to-air mass ratio (F/A) was 0.00345, which is quite lean, and apparently the primary air flow dominates the flow structure. As observed in Figs. 17 and 18, the combustion is limited to the radial positions greater than 1 in. and to axial regions within 10.5 in. of the nozzle exit plane. The inner air core remains relatively cool until axial positions beyond 21 in. are reached, at which point it appears that the hot combustion gases and the air flow mix together to achieve a uniform gas temperature of $\approx 550 \text{ K}$. For DTINDR = 10, the F/A was increased to 0.107. The combustion process begins quite early for this configuration (axial position $\leq 2.5 \text{ in.}$) and very close to the boundary between the primary air flow and the H_2 flow. The primary air core remains cool until an axial position of 5.25 in.; however, beyond this position, the temperature of the central core progressively rises as the combustion process continues and shifts to the central region of the flow. In contrast to the DTINDR = 2 configuration, average temperatures on the centerline rise to nearly 1400 K.

The axial centerline variation of air number density (see Fig. 24) also indicates a significant difference between the two test configurations. For DTINDR = 2.0, the air number density on the axial centerline remains nearly constant out to the 24-in. axial position, at which point it begins to decrease as centerline temperatures begin to increase. In contrast, the axial centerline air number density for DTINDR = 10.0 rapidly decreases with axial distance from the nozzle exit.

4.4 COMPARISON OF THE RESULTS WITH CALCULATIONS

Equilibrium chemistry calculations were available only for the DTINDR = 10.0 configuration. As shown in Figs. 19 and 20, the measured temperature values disagree markedly with the equilibrium chemistry predictions. At the axial position of 2.5 in., a peak average temperature of 1900 K is predicted within 0.25 in. of the axial centerline. Measurements show a peak temperature of 1100 K at the 0.6-in. radial position. Similar disagreements are observed in other axial positions. However, the measured temperature profile at the 26.25-in. axial position indicates that measurements and predictions for large axial positions are beginning to move toward agreement. Furthermore, the measured air number densities at the 21- and 26.25-in. axial positions bracket the predictions of N_2 number density as shown in Fig. 23.

5.0 SUMMARY

The laser-Raman technique has been successfully used to partially map the flow field of an H_2 /air combustor for two widely different test conditions. The system performed admirably under what must truly be described as hostile conditions. The test cell area was hot and humid (as a result of the water spray coolers) during operation as well as dirty and dusty at all times. As a result of energy conservation measures, the equipment was frequently exposed to subfreezing temperatures when not in use. Furthermore, during one test period, the viewport was blown out twice during combustion ignition, but the optical system was only slightly damaged. As there were many possibilities for equipment malfunction to result directly from the test cell area environment, it is a credit to the durability of the system that only moderate, easily corrected, electro-optical-mechanical difficulties were encountered.

The original experiment plan included mapping the flow-field H_2 density and N_2 density using the H_2 rotational lines and the N_2 vibration-rotation band, respectively. In addition the H_2 rotational lines were to be used to provide more accurate determination of temperature in regions of high H_2 /low N_2 concentrations. However, limited resources prevented making these measurements. As a result, the measurement uncertainties are much higher than expected, and this limits the usefulness of the data for combustion modeling. However, a further analysis of the data [i.e., comparisons with flow-field parameter calculations, pressure probe measurements, infrared (IR) measurements, and laser velocimeter measurements] can reduce the uncertainty of the Raman measurements by providing a more accurate estimate of the N_2/O_2 mole fraction ratio. Although such analysis is beyond the scope of this report, the following conclusions/observations can be made for these experiments:

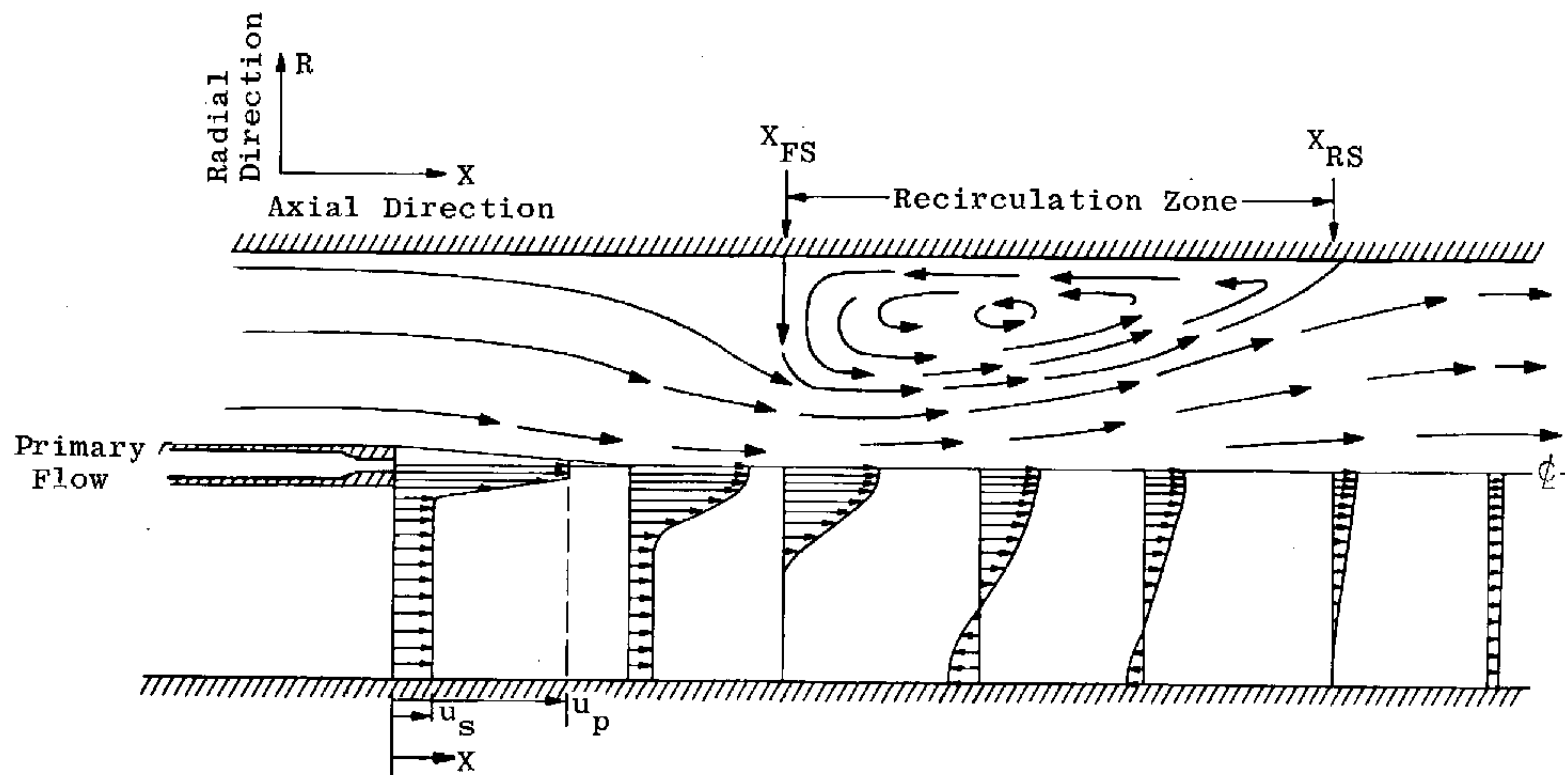
1. One of the main impediments to faster data acquisition was the poor performance of the hydraulic scanning table on which the laser-Raman optical system was mounted. This table should be replaced by one that is sturdier and more capable of easy, accurate, and rapid positioning.
2. Background radiation from the flow field was undetectable because of the cleanliness of the flow field. The absence of particulates also eliminated laser-induced particulate incandescence, which would have been manifested by off-band radiation during laser firings.
3. In the high-temperature zones of the flow fields, instantaneous temperature values approached the expected peak level of $\simeq 2500$ K. However, average temperature values were never higher than 1500 K. The spatial resolution of the measurements may not have been sufficient to resolve the peak temperature zones. Furthermore, if the turbulence frequency reaches the order of kilohertz, then the number of samples used for a data point must be increased by nearly two orders of magnitude to obtain a more reliable average temperature.
4. For the DTINDR = 2 configuration, the peak combustion zone is near the 5.21-in. position, and the highest average temperature ($\simeq 1400$ K) occurs there near the test cell wall. Axial centerline temperatures begin to increase only at the 21.07-in. axial position, and the flow appears to be uniform with a nominal temperature of 550 K by the 31.5-in. axial position.
5. The peak combustion zone is much more difficult to define for the DTINDR = 10 configuration. Temperatures as high as 1100 K were found at the 2.59-in. axial position and within 1 in. of the axial centerline followed by decreasing temperatures toward the test cell wall. Centerline temperatures rapidly increased as axial distance from the nozzle increased; even at the 26.27-in. axial position, the flow core was at 1400 K, with temperatures decreasing toward the test cell wall.
6. For the DTINDR = 2 configuration, the number density radial distribution at the 0.55-in. axial position shows the broad uniform core of the air flow corresponding to the 1.31-in. radius of the primary nozzle. Beyond the 1.31-in. radial position, the number density profile exhibits a "sawtooth" behavior that corresponds to the secondary flow hole-separation in the baffle plate.

7. For the DTINDR = 10 configuration, the nearest axial position at which a radial scan was made was 2.6 in. At this position the H₂ secondary flow intruded into the primary air flow. Even so, the primary air flow core corresponding to the 0.262-in. radius of the primary nozzle is well-defined. Within 0.5 in. of the axial centerline, the H₂ concentration increased by nearly two orders of magnitude.
8. The general trend of the number density radial profiles for the DTINDR = 2 configuration is a broad, uniform air core with decreasing number density toward the test cell wall. For the DTINDR = 10 configuration, the number density scans at axial positions of 10.44 in. or less have a U-shaped profile. That is, the number densities decrease from the central core value, bottom out, and then gradually increase toward the test cell wall.
9. Equilibrium chemistry calculations for the DTINDR = 10 configuration fail to predict the observed temperature and density profiles for axial positions of 15.75 in. or less. However, for the 21.02- and 26.27-in. axial positions, the measurements and predictions agree to within ± 20 percent.

REFERENCES

1. Chriss, D. E. "An Experimental Investigation of Ducted, Reactive, Turbulent Jet Mixing with Recirculation." AEDC-TR-77-56 (ADA044110), September 1977.
2. Schulz, R. J. "An Investigation of Ducted, Two-Stream, Variable-Density, Turbulent Jet Mixing with Recirculation." AEDC-TR-76-152 (AD-A034537), January 1977.
3. Placzek, G. "The Rayleigh and Raman Scattering." Translated from a publication of the Akademische Verlags Gesellschaft G. M. B. H., Leipzig, 1934, *Handbuch der Radiologie*, Heft 6, Teil 2, pp. 209-374.
4. Placzek, G. and Teller, E. "Die Potationsstruktur der Ramanbanden Mehratomiger Moleküle." *Zeitschrift für Physik*, Vol. 81, March 1933.
5. Sushchinskii, M. M. *Raman Spectra of Molecules and Crystals*. Israel Program for Scientific Translations, New York, 1972.
6. Anderson, A., ed. *The Raman Effect*. Vol. 2. Marcel Dekker, Inc., New York, 1973.
7. Drake, M. C. and Rosenblatt, G. M. "Rotational Raman Scattering from Premixed and Diffusion Flames." *Combustion and Flame*, Vol 33, No. 2, October 1978, pp. 179-196.

8. Eckbreth, A. C., Bonczyk, P. A., and Verdieck, J. F. "Review of Laser Raman and Fluorescence Techniques for Practical Combustion Diagnostics." UTRC-R77-952665-6, February 1977.
9. Eckbreth, A. C. "Averaging Considerations for Pulsed, Laser Raman Signals from Turbulent Combustion Media." *Combustion and Flame*, Vol. 31, No. 3, 1978, pp. 231-237.



u_p is the primary jet velocity at nozzle exit.

u_s is the secondary jet velocity at nozzle exit.

Mean streamline pattern shown in upper half figure.

Mean axial velocity profiles shown in lower half figure.

Figure 1. Turbulent, ducted, mixing system with recirculation.

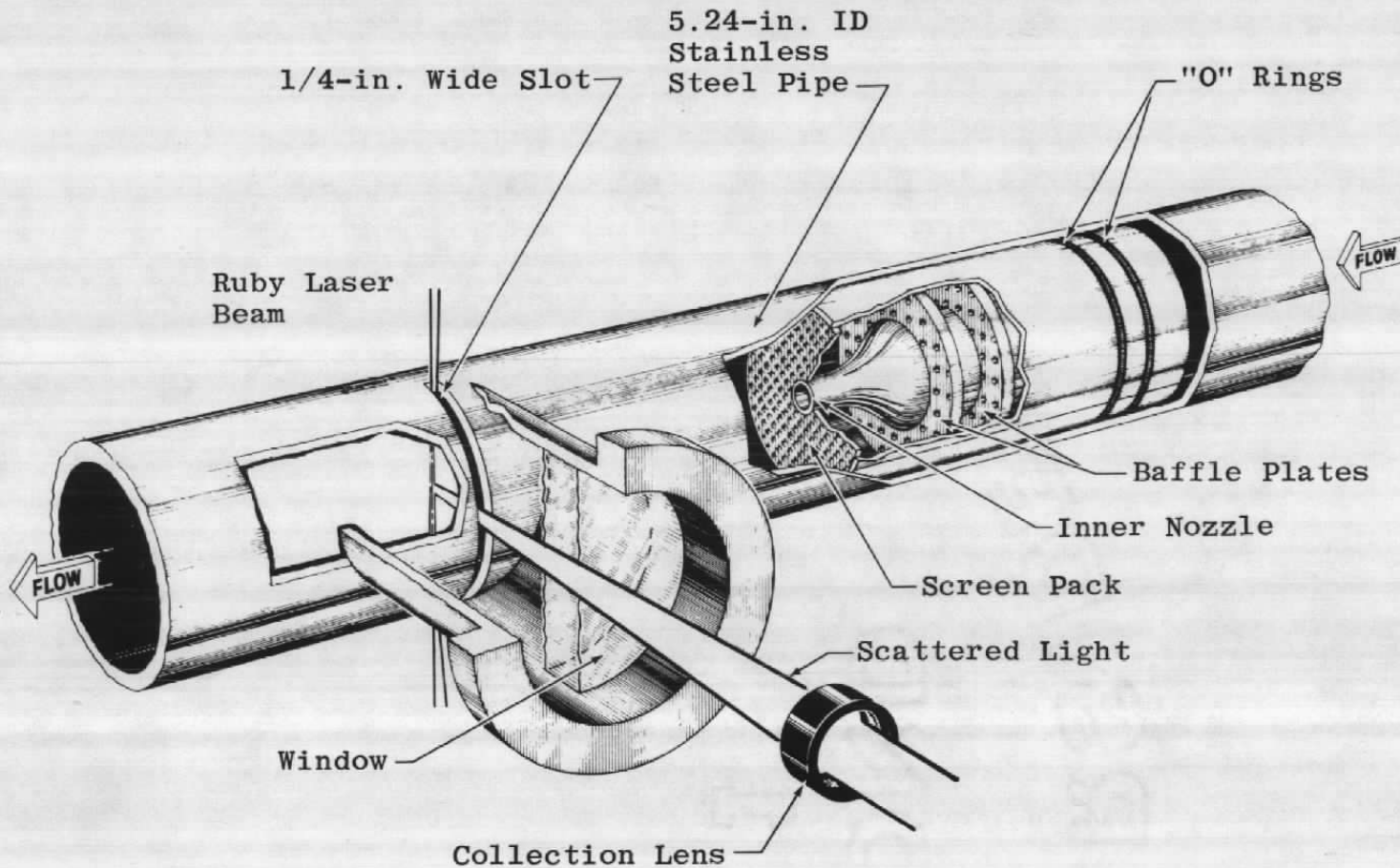


Figure 2. Recirculating flow combustor simulation facility.

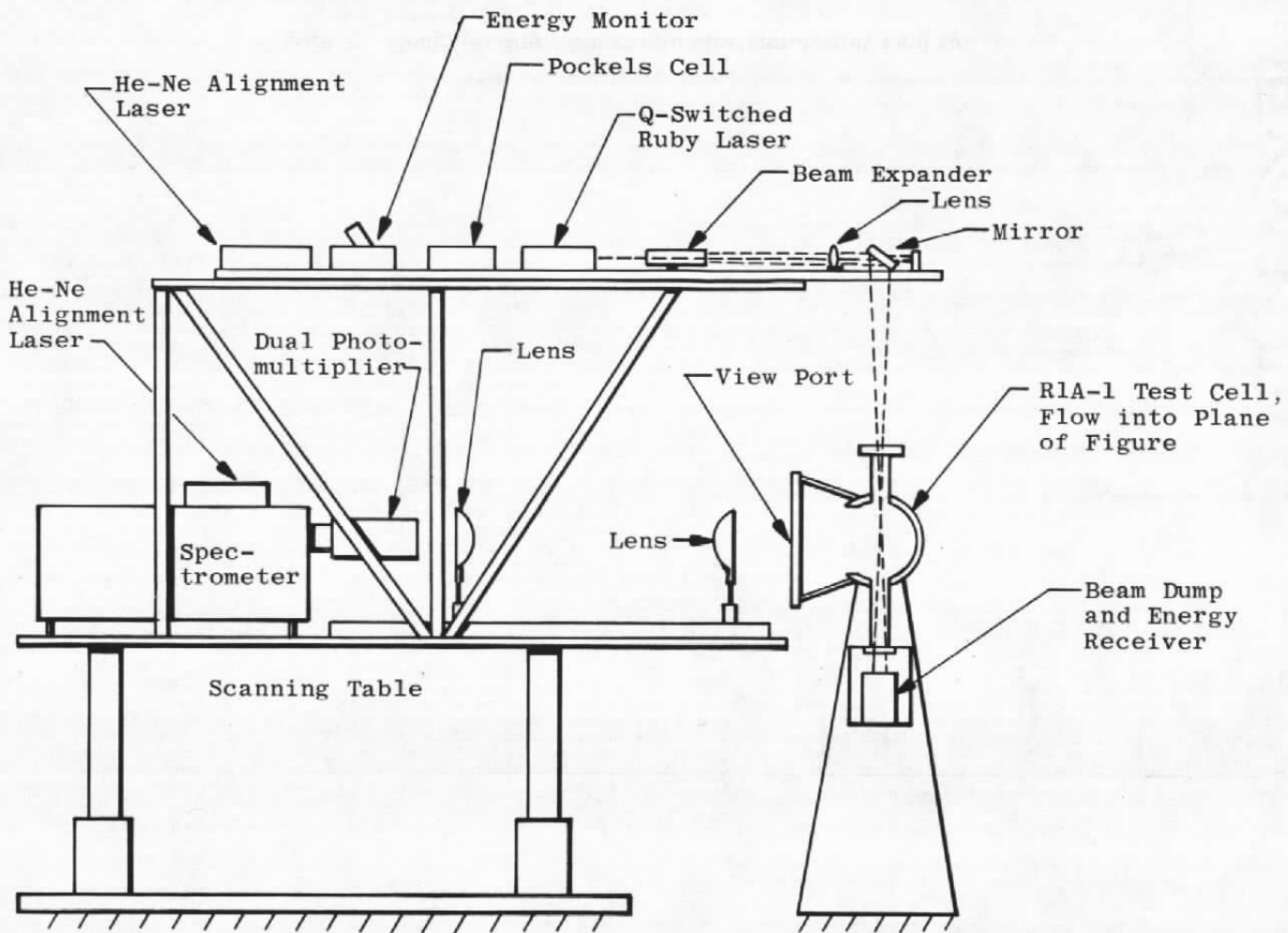
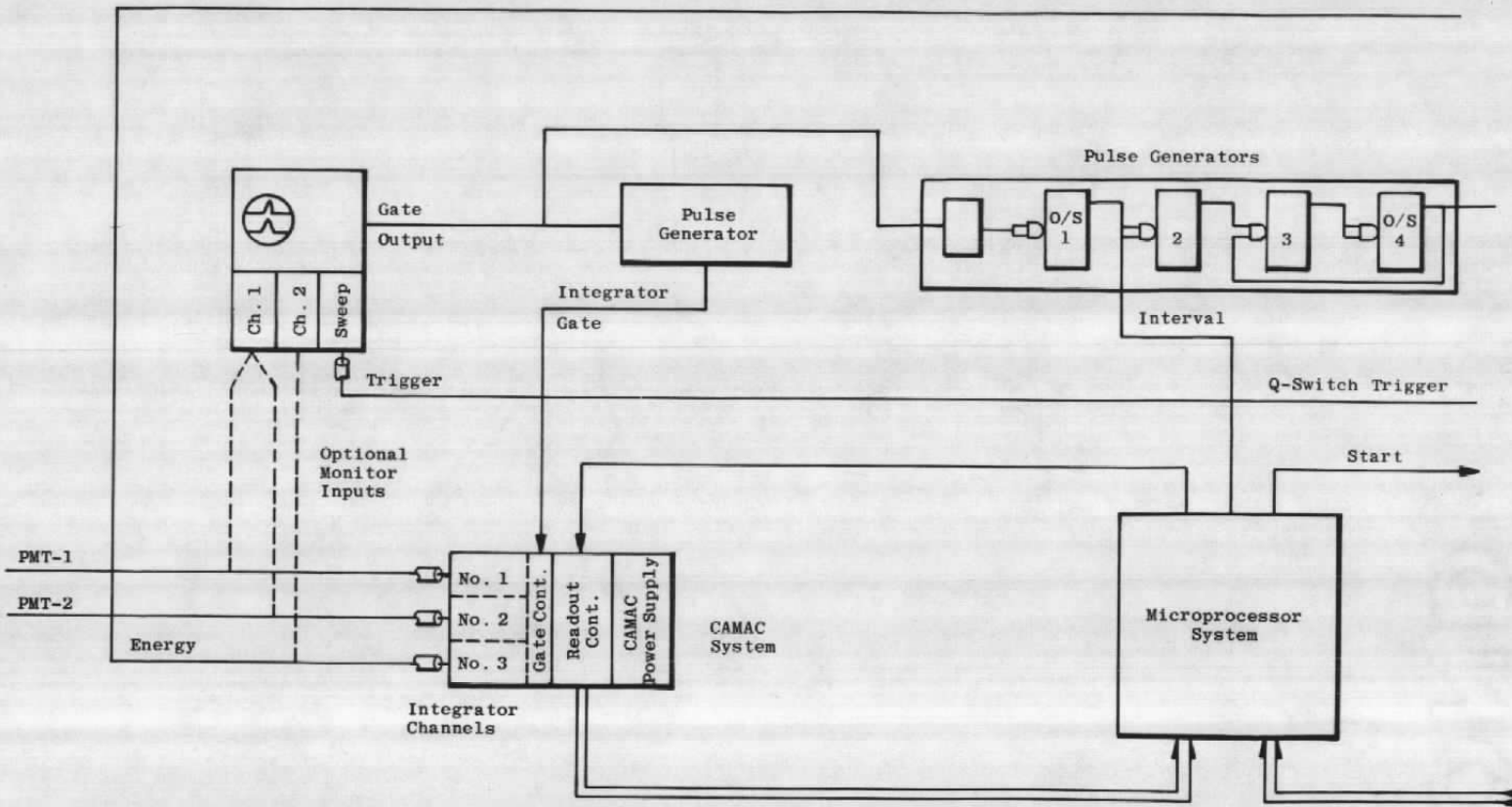
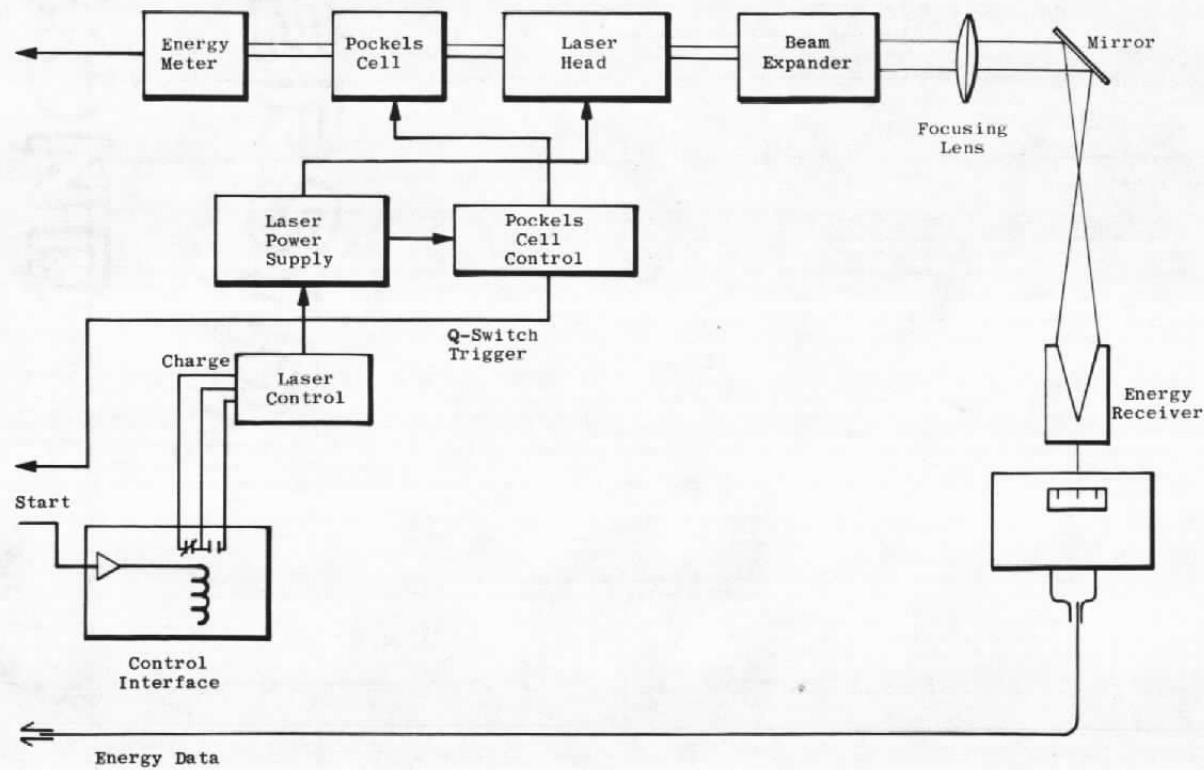


Figure 3. Laser-Raman experimental configuration at AEDC-ETF Research Cell R1A1.



a. Data acquisition electronics

Figure 4. Block diagram of electronic systems applicable during the data acquisition interval, Q-switch/integrator technique.



b. Laser system electronics
Figure 4. Concluded.

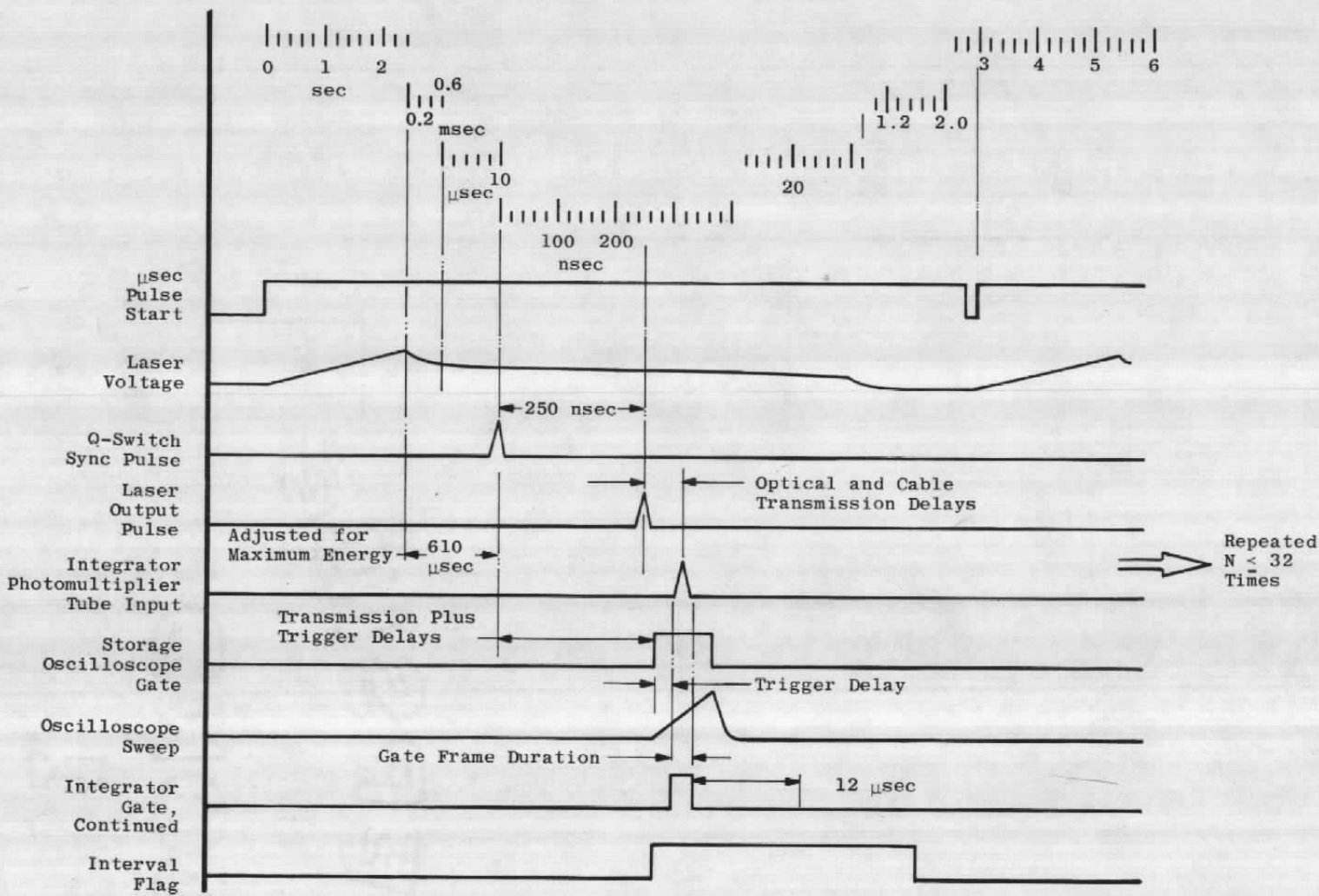


Figure 5. Typical timing diagram for data acquisition sequence.

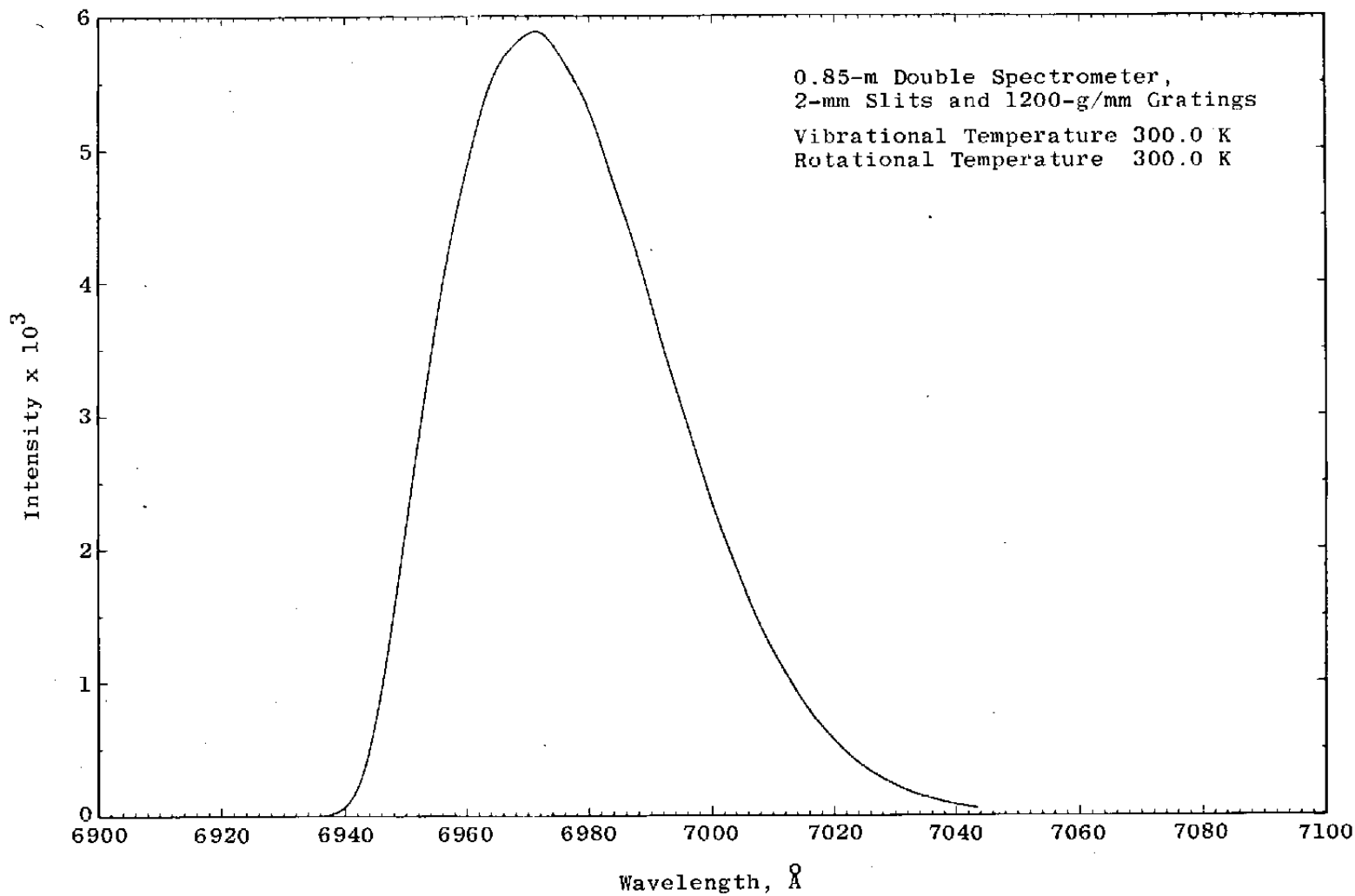


Figure 6. Pure rotational Raman spectrum, N_2 and O_2 at $T = 300$ K;
 $[\text{N}_2]/[\text{O}_2] = 3.73$.

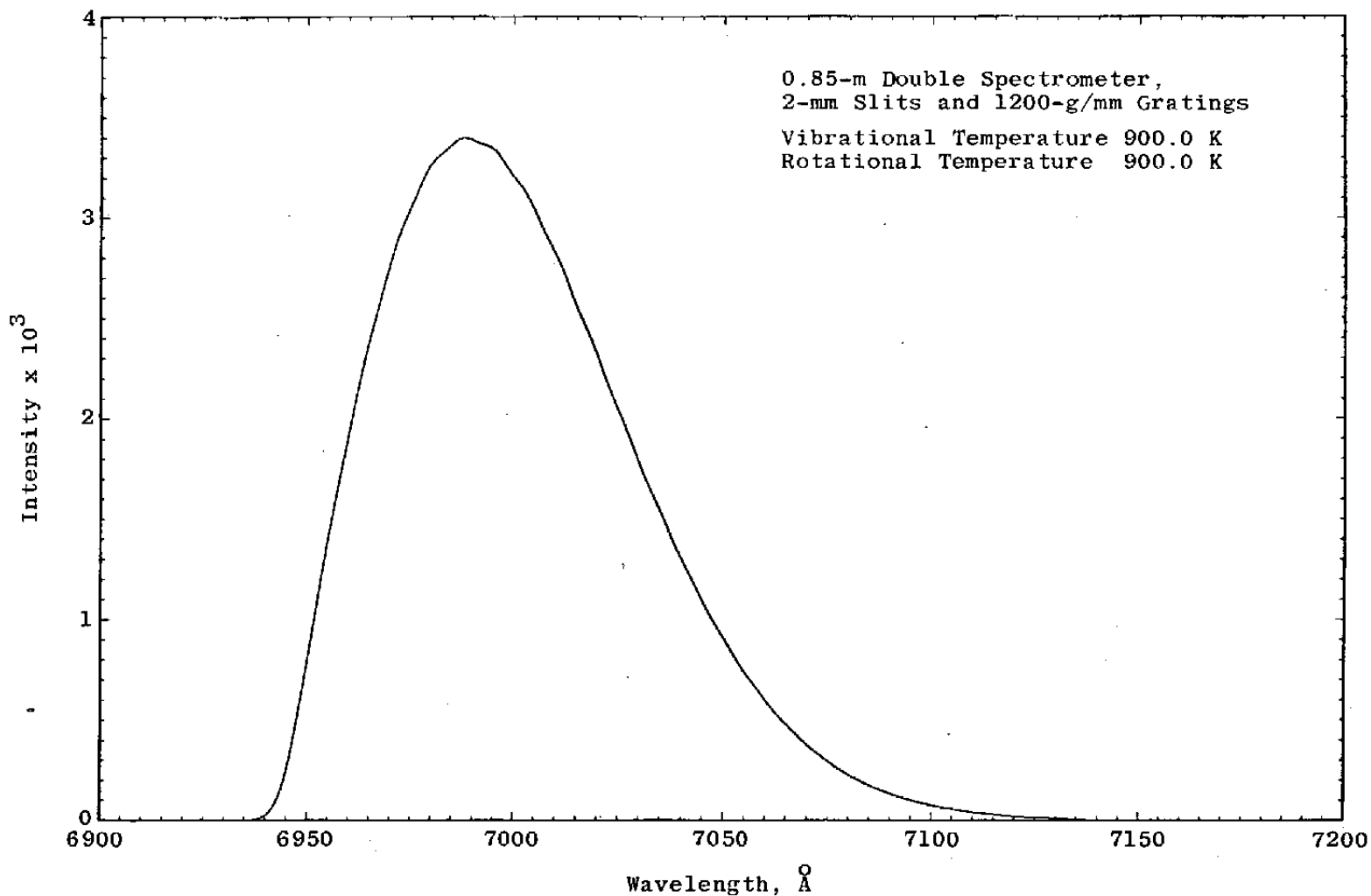


Figure 7. Pure rotational Raman spectrum, N_2 and O_2 at $T = 900$ K;
 $[\text{N}_2]/[\text{O}_2] = 3.73$.

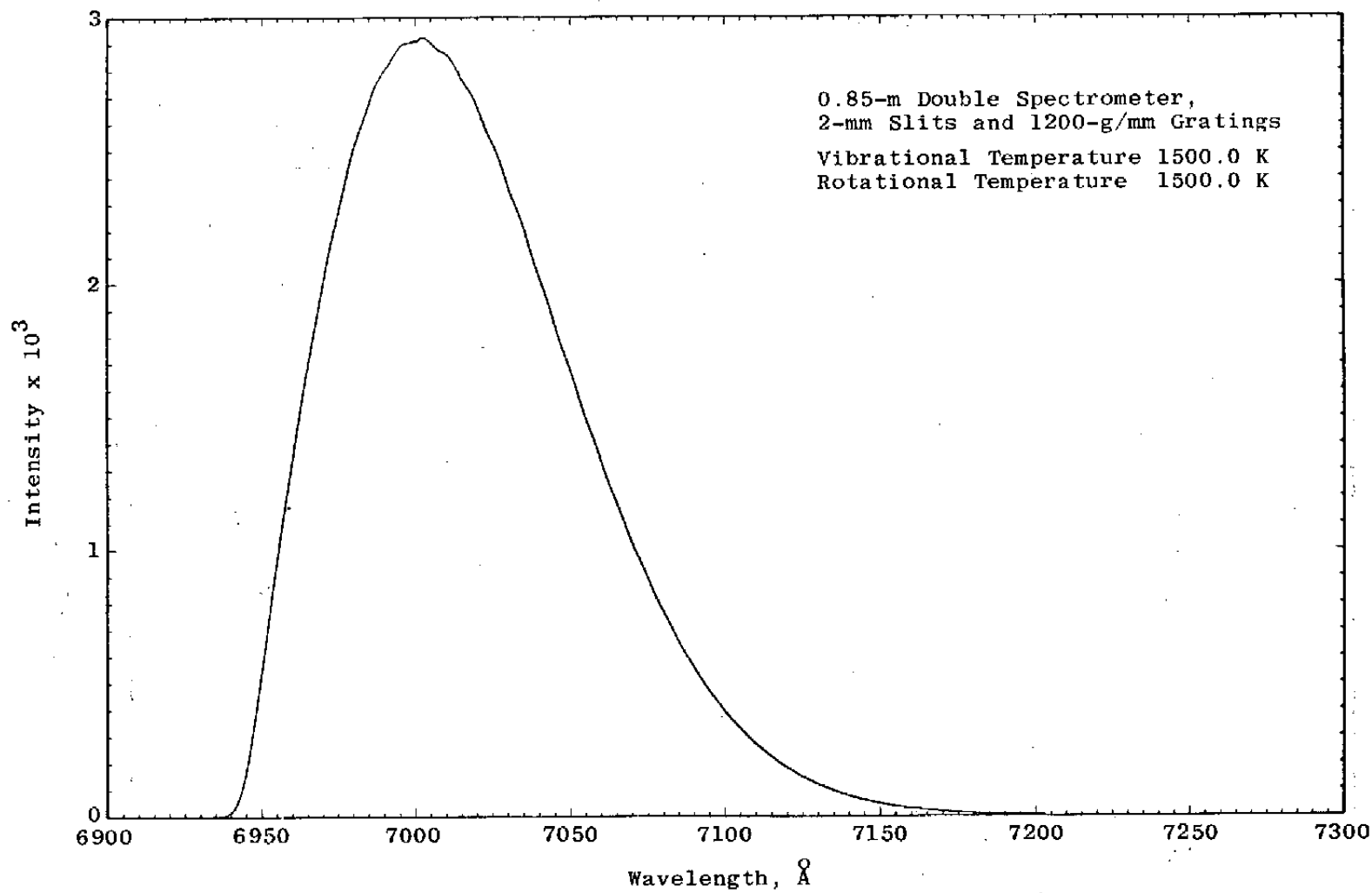


Figure 8. Pure rotational Raman spectrum, N_2 and O_2 at $T = 1500$ K;
 $[\text{N}_2]/[\text{O}_2] = 3.73$.

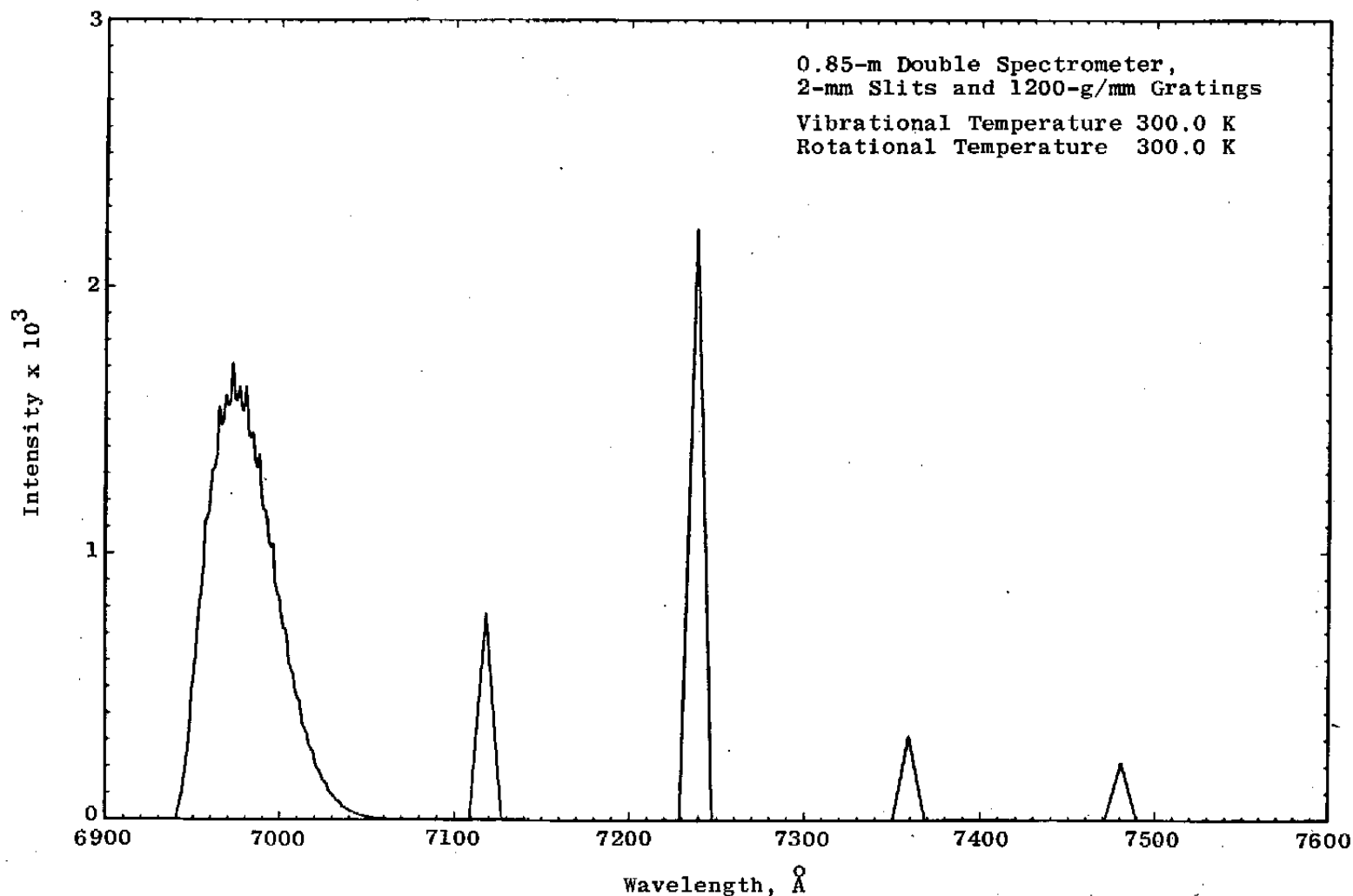


Figure 9. Pure rotational Raman spectrum, N_2 and H_2 at $T = 300$ K;
 $[\text{N}_2]/[\text{H}_2] = 0.667$.

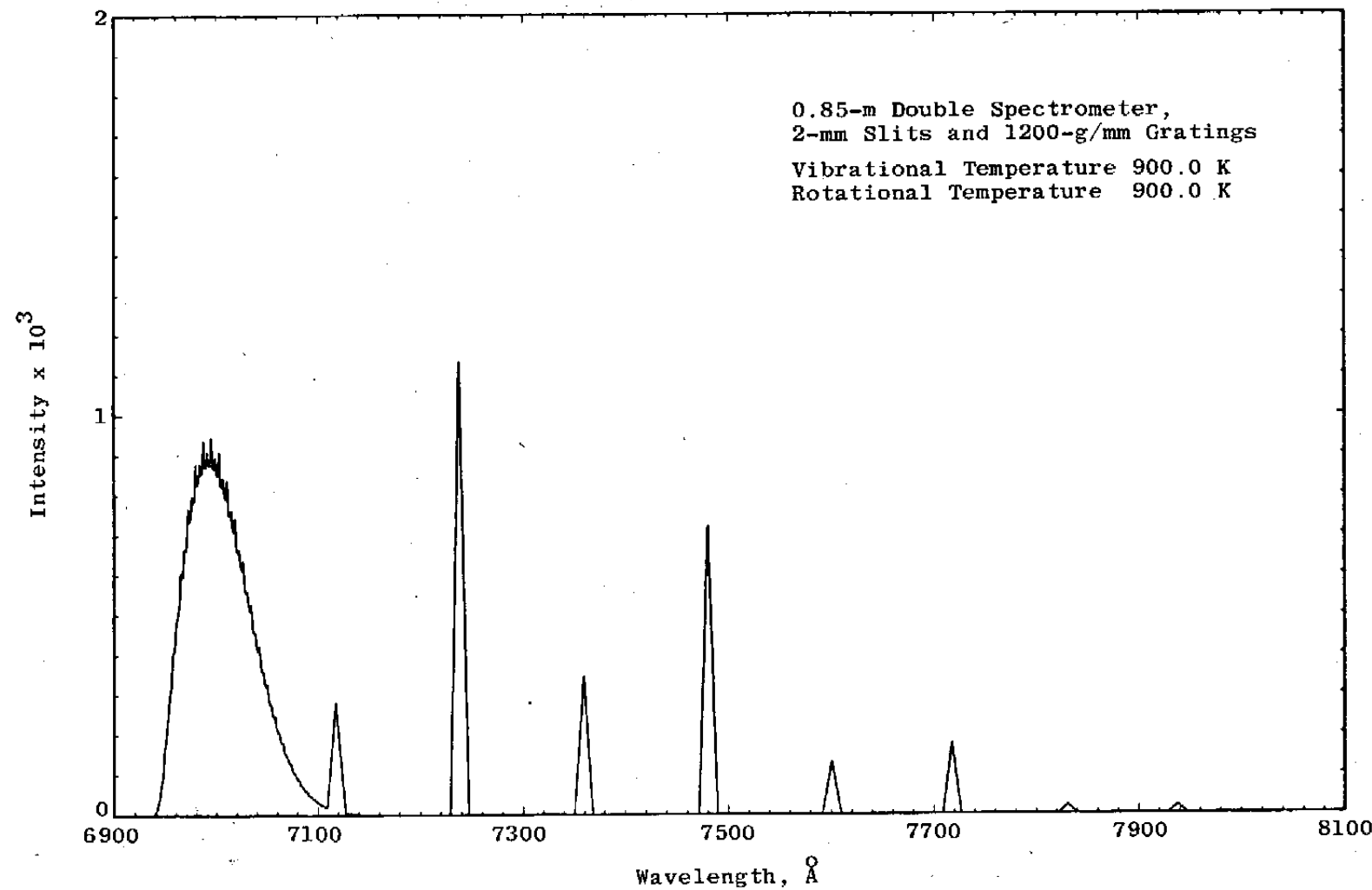


Figure 10. Pure rotational Raman spectrum, N_2 and H_2 at $T = 900 \text{ K}$;
 $[\text{N}_2]/[\text{H}_2] = 0.667$.

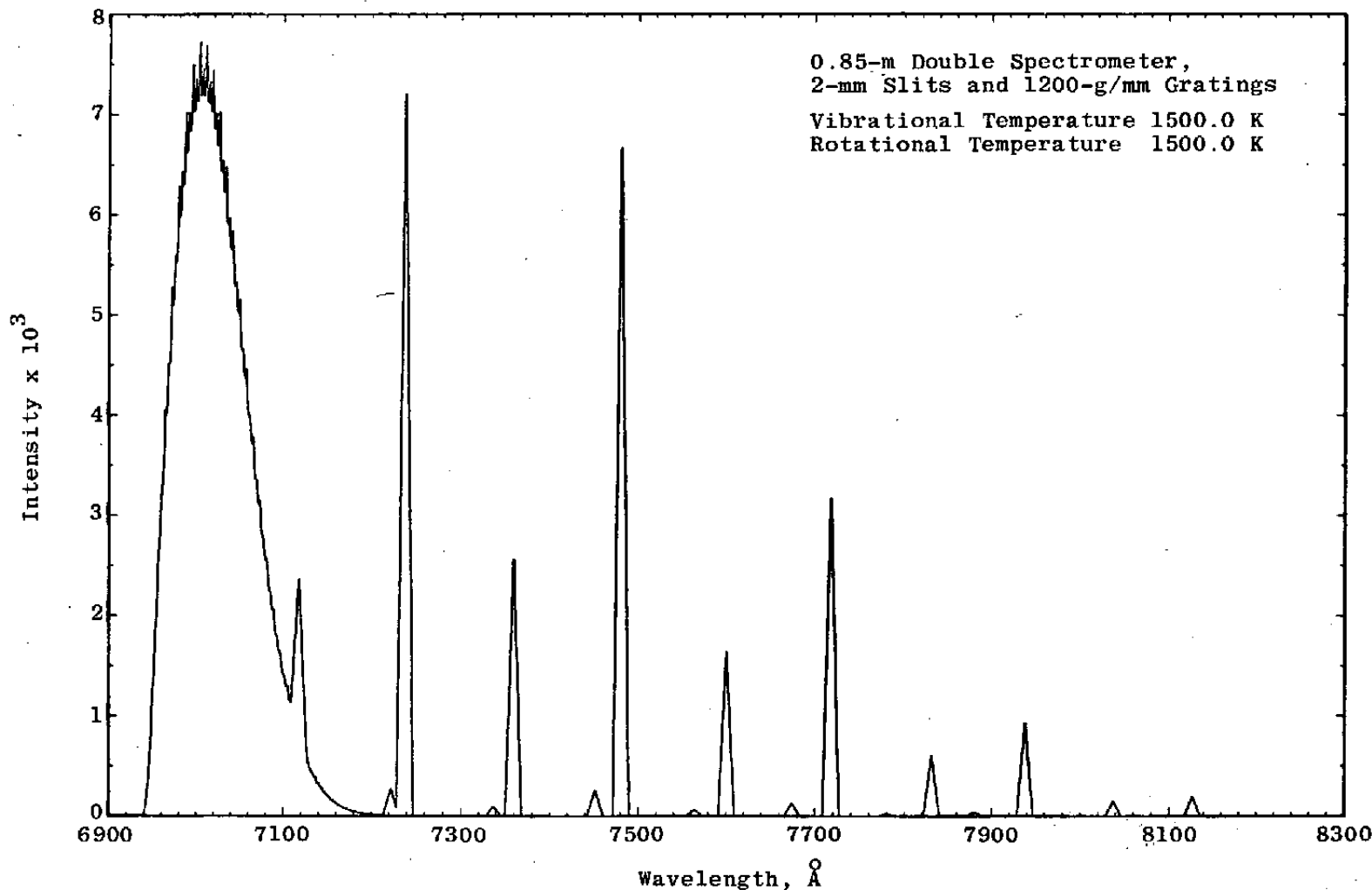


Figure 11. Pure rotational Raman spectrum, N_2 and H_2 at $T = 1500$ K;
 $[\text{N}_2]/[\text{H}_2] = 0.667$.

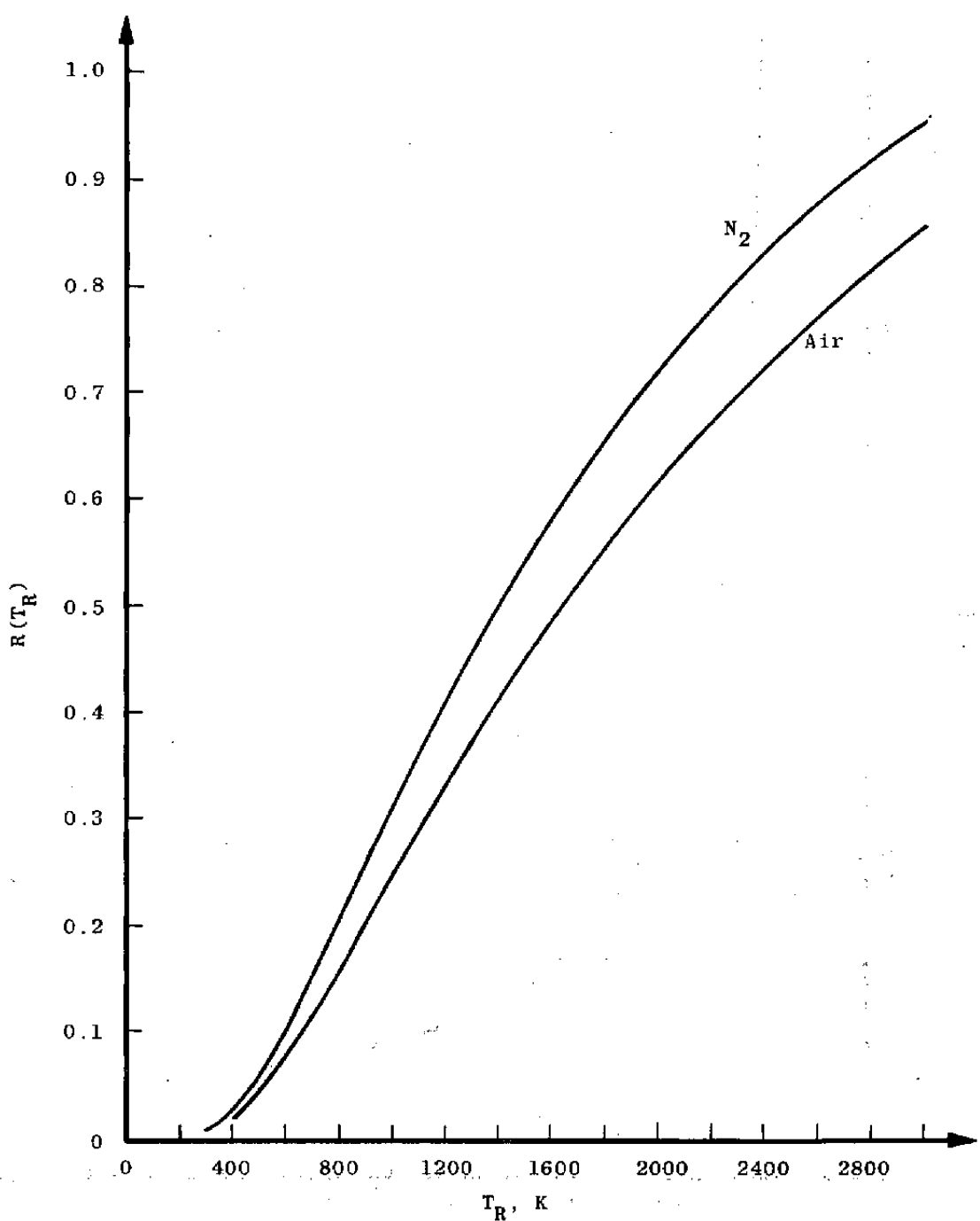


Figure 12. Intensity ratio, $I_c(7061 \text{ \AA})/I_c(7010 \text{ \AA})$, as a function of temperature.

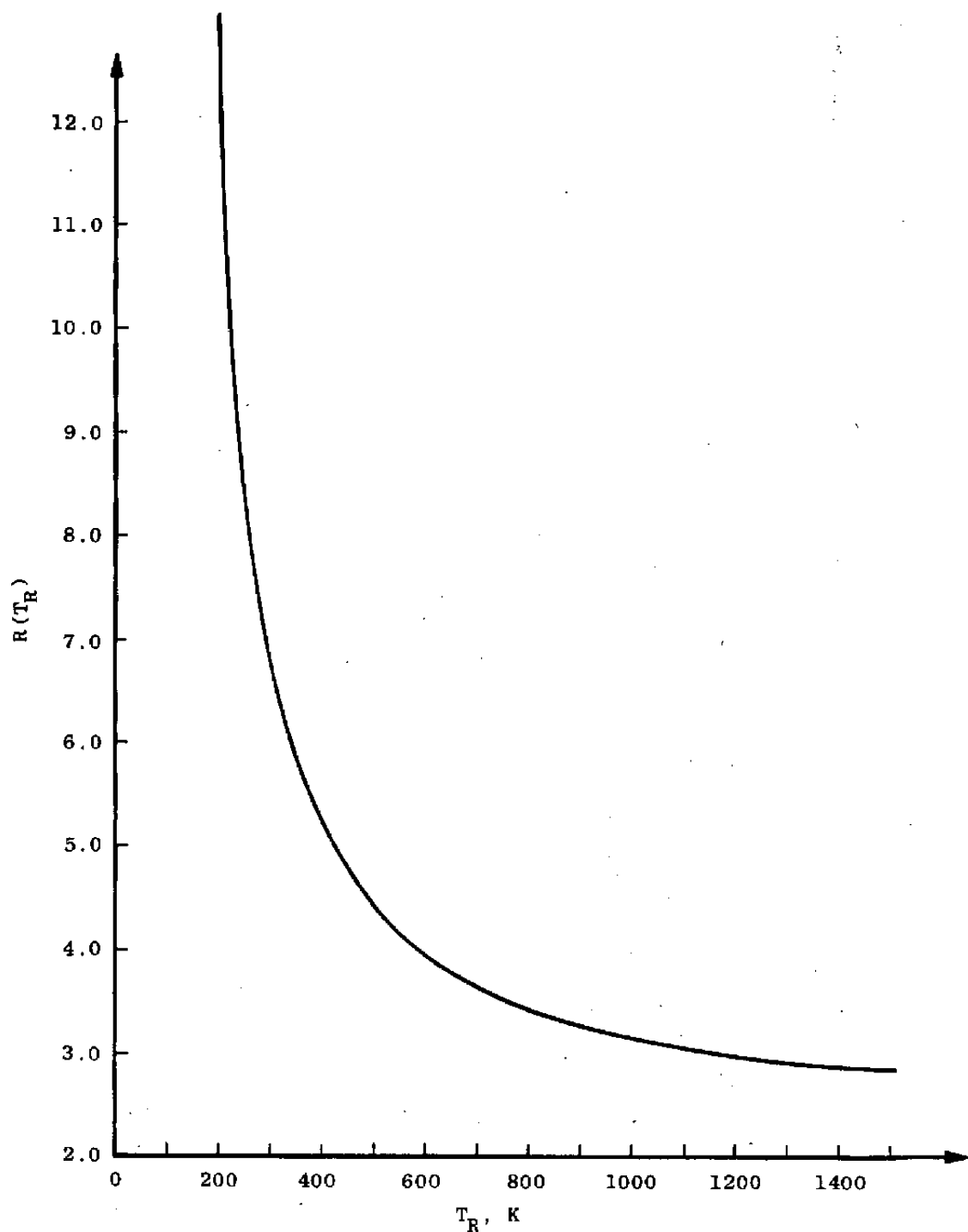


Figure 13. Intensity ratio, $I_c(J = 1, H_2)/I_c(J = 2, H_2)$, as a function of temperature.

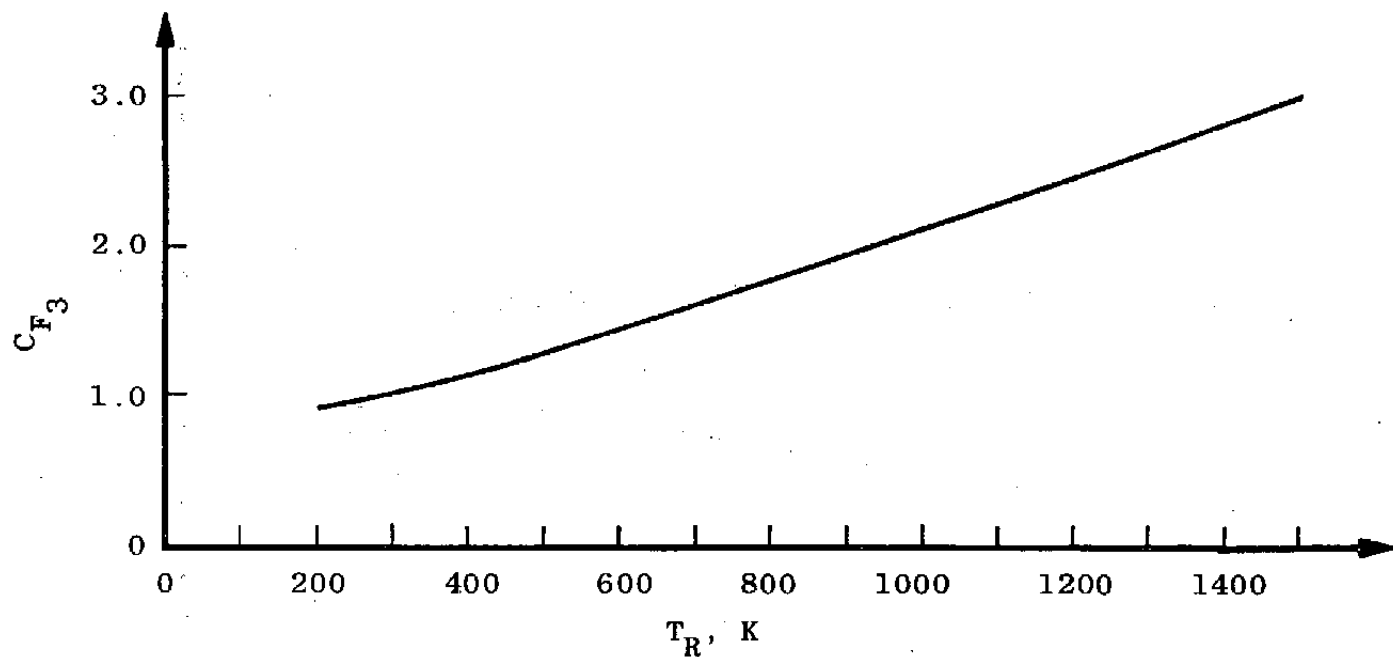


Figure 14. $J = 1$, H_2 line intensity relative temperature dependence.

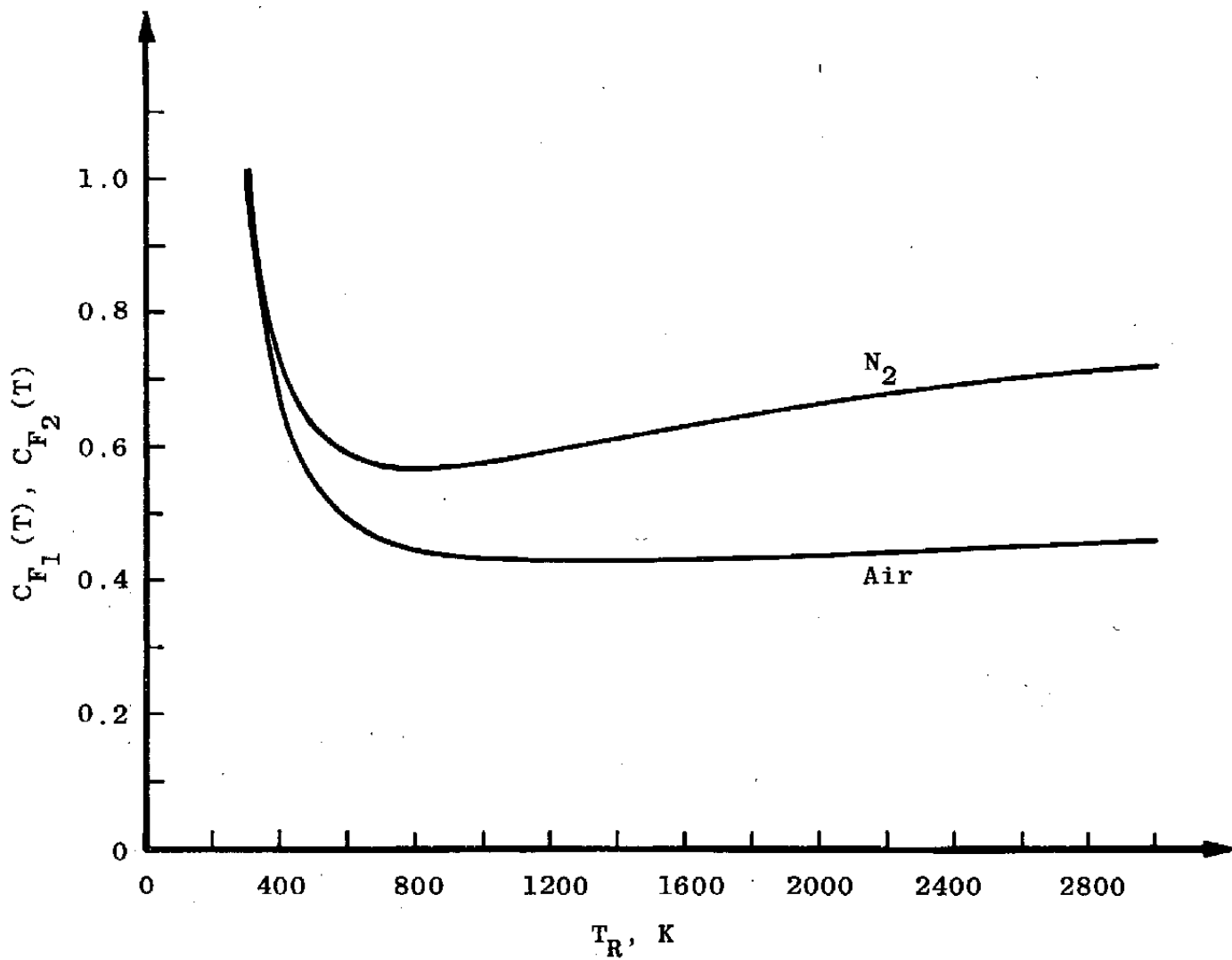


Figure 15. I_c (7010 Å) relative temperature dependence.

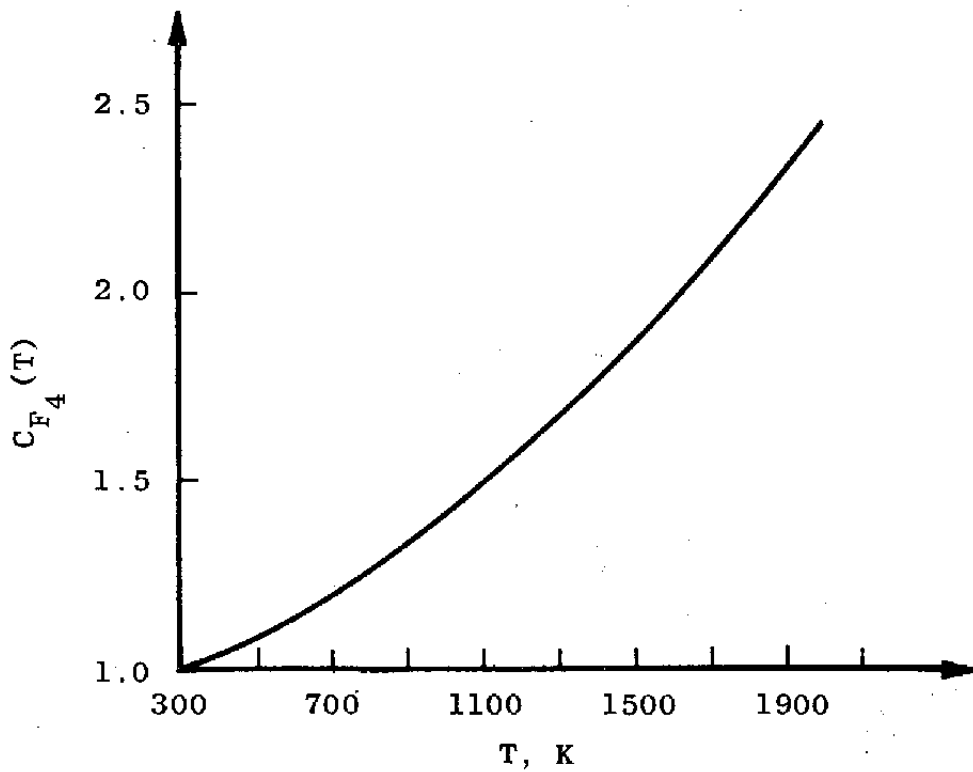


Figure 16. N_2 vibration-rotation band, Q-Branch intensity relative temperature dependence.

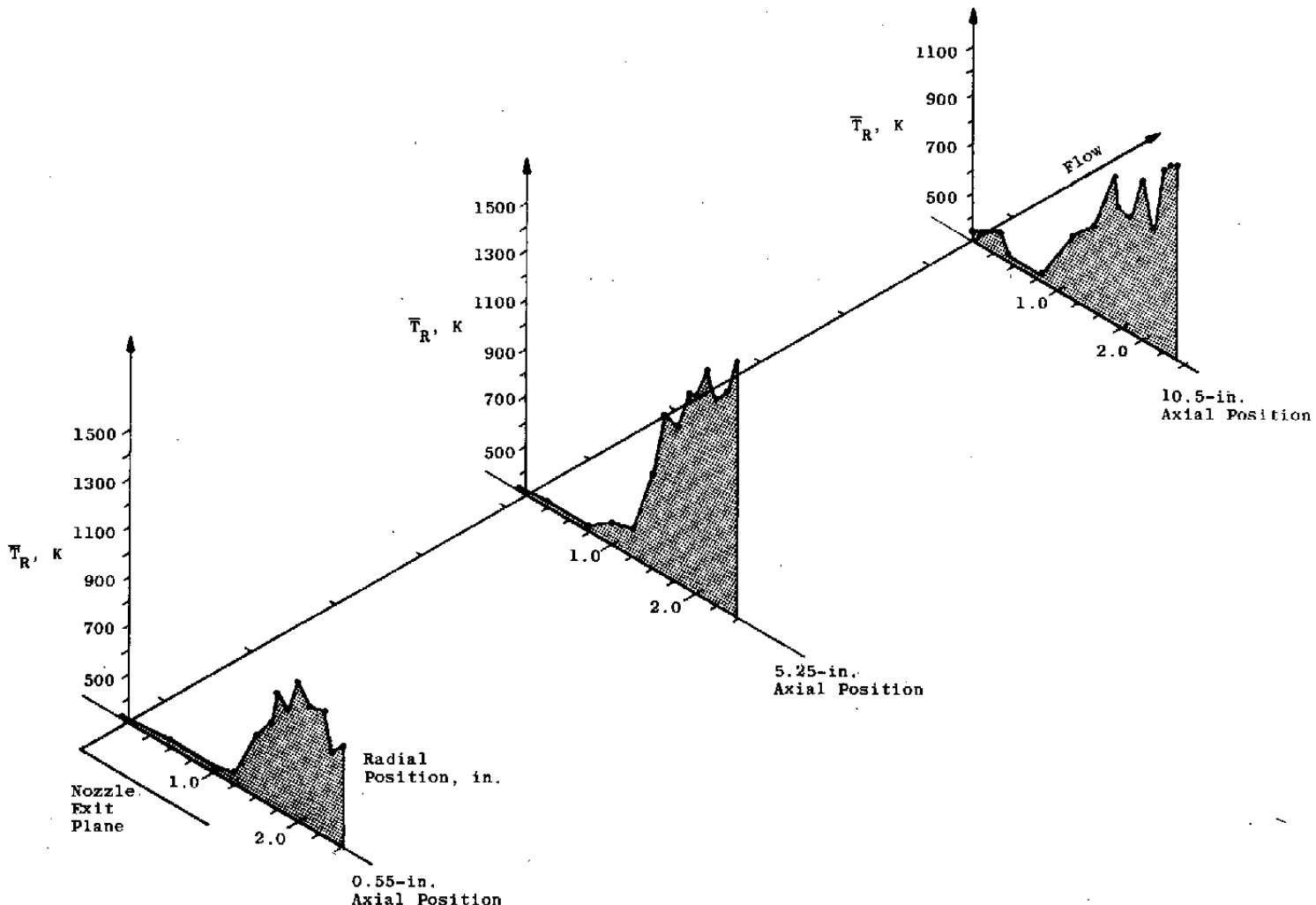


Figure 17. Isometric plot of measured radial temperature distribution,
DTINDR = 2; 0.55-, 5.25-, 10.5-in. axial positions.

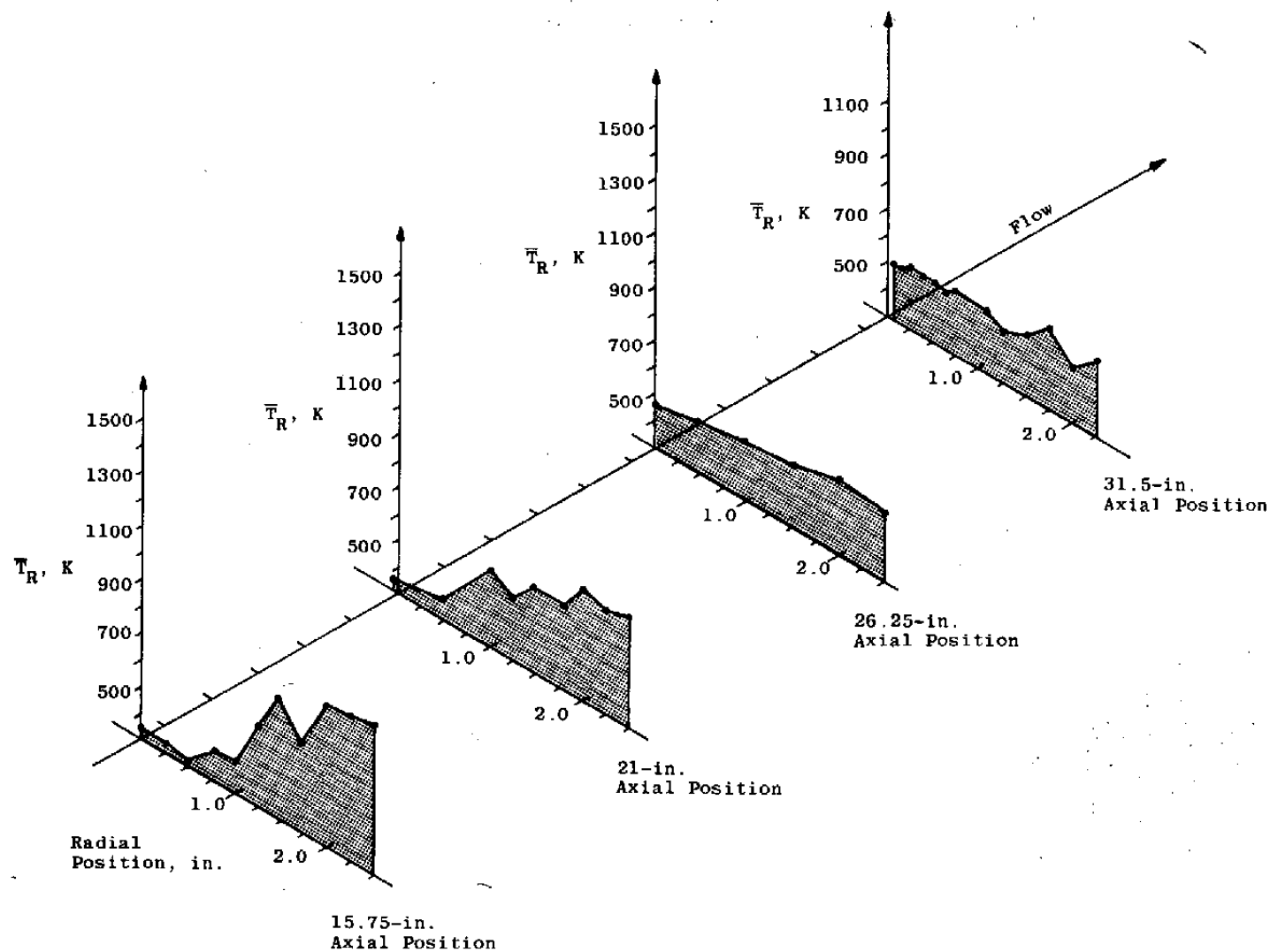


Figure 18. Isometric plot of measured radial temperature distribution,
DTINDR = 2; 15.75-, 21-, 26.25-, 31.5-in. axial positions.

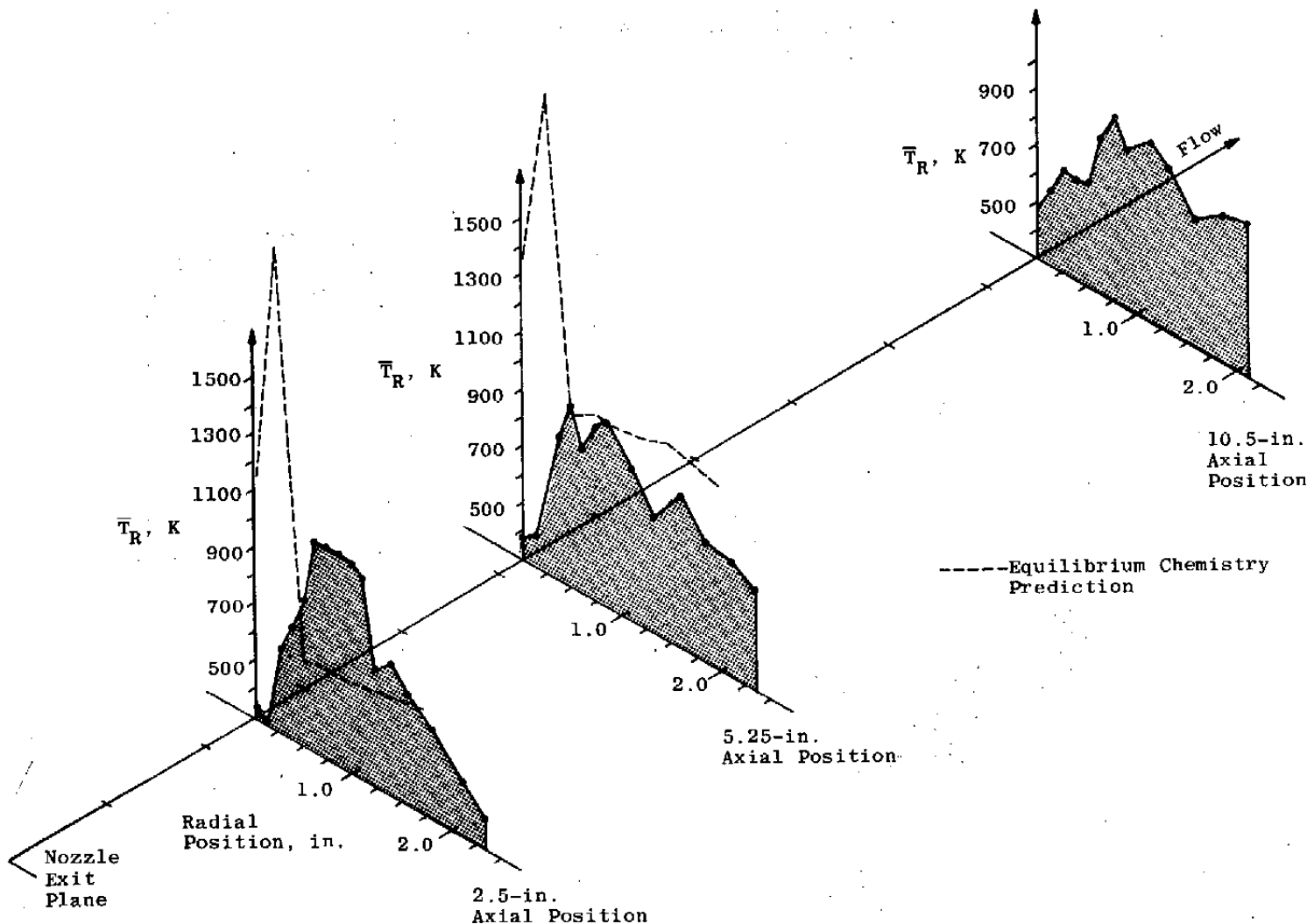


Figure 19. Isometric plot of measured radial temperature distribution,
DTINDR = 10; 2.5-, 5.25-, 10.5-in. axial positions.

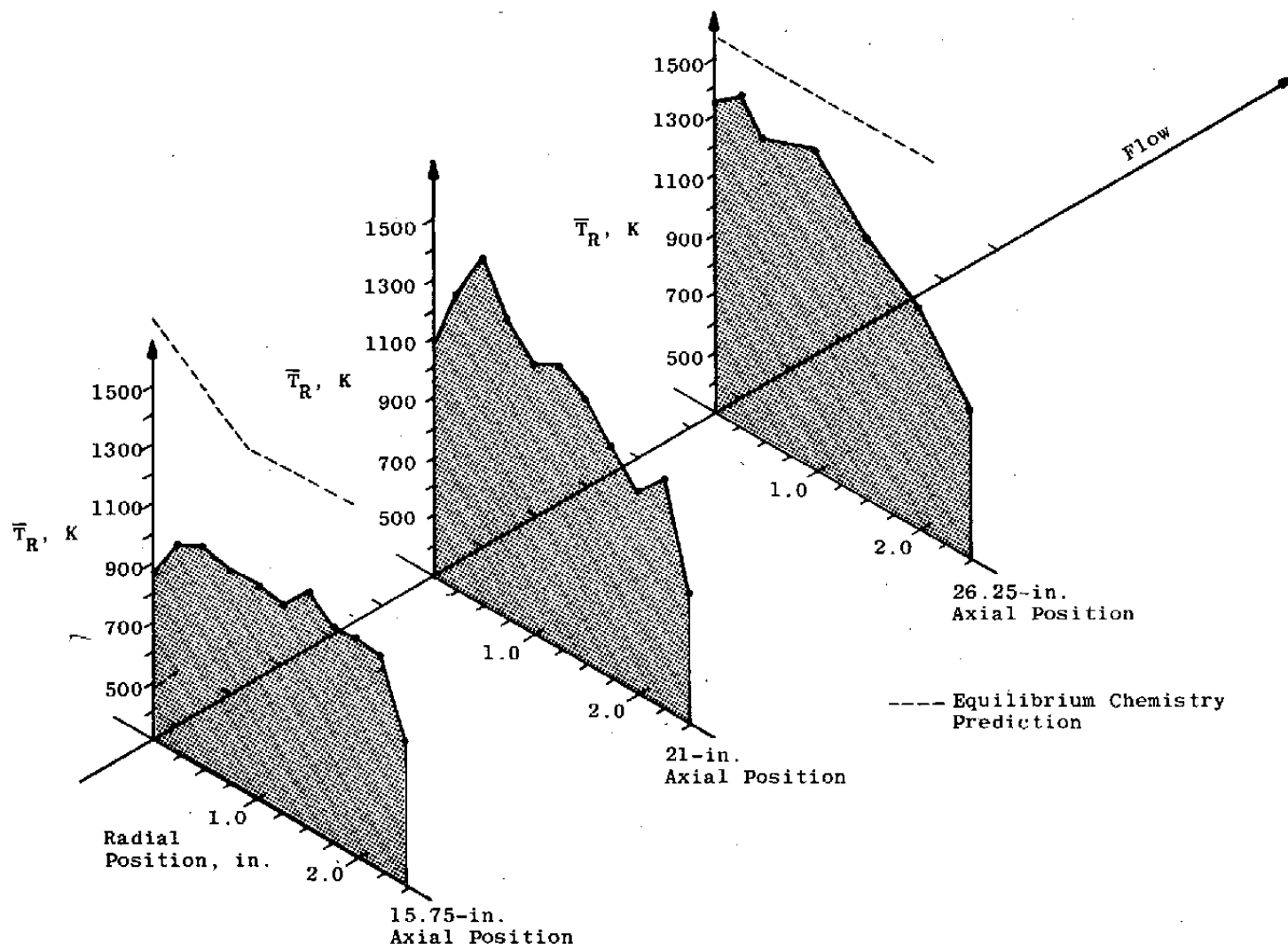


Figure 20. Isometric plot of measured radial temperature distribution, DTINDR = 10; 15.75-, 21-, 26.25-in. axial positions.

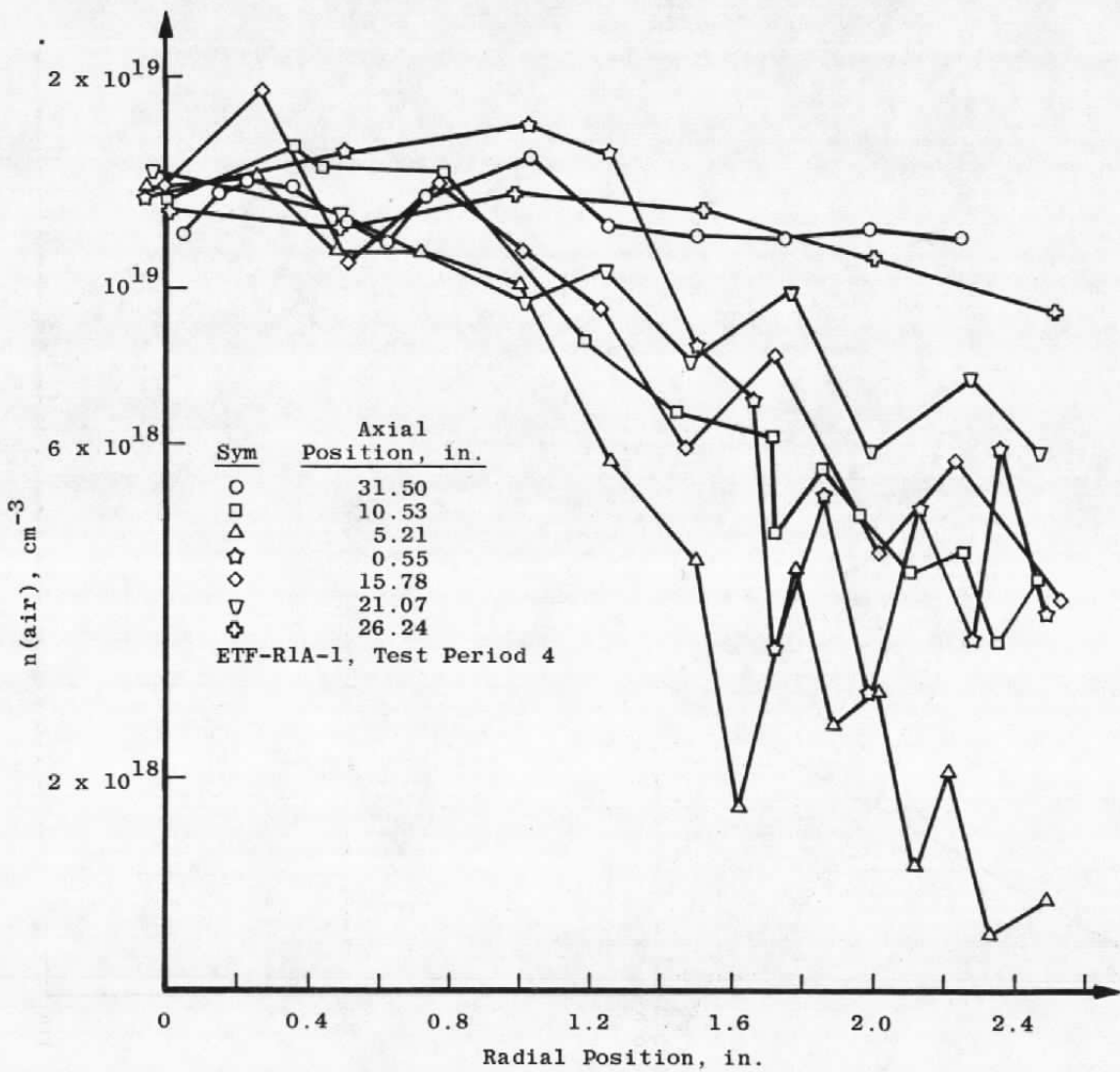


Figure 21. Air number density as a function of flow-field position, DTINDR = 2.

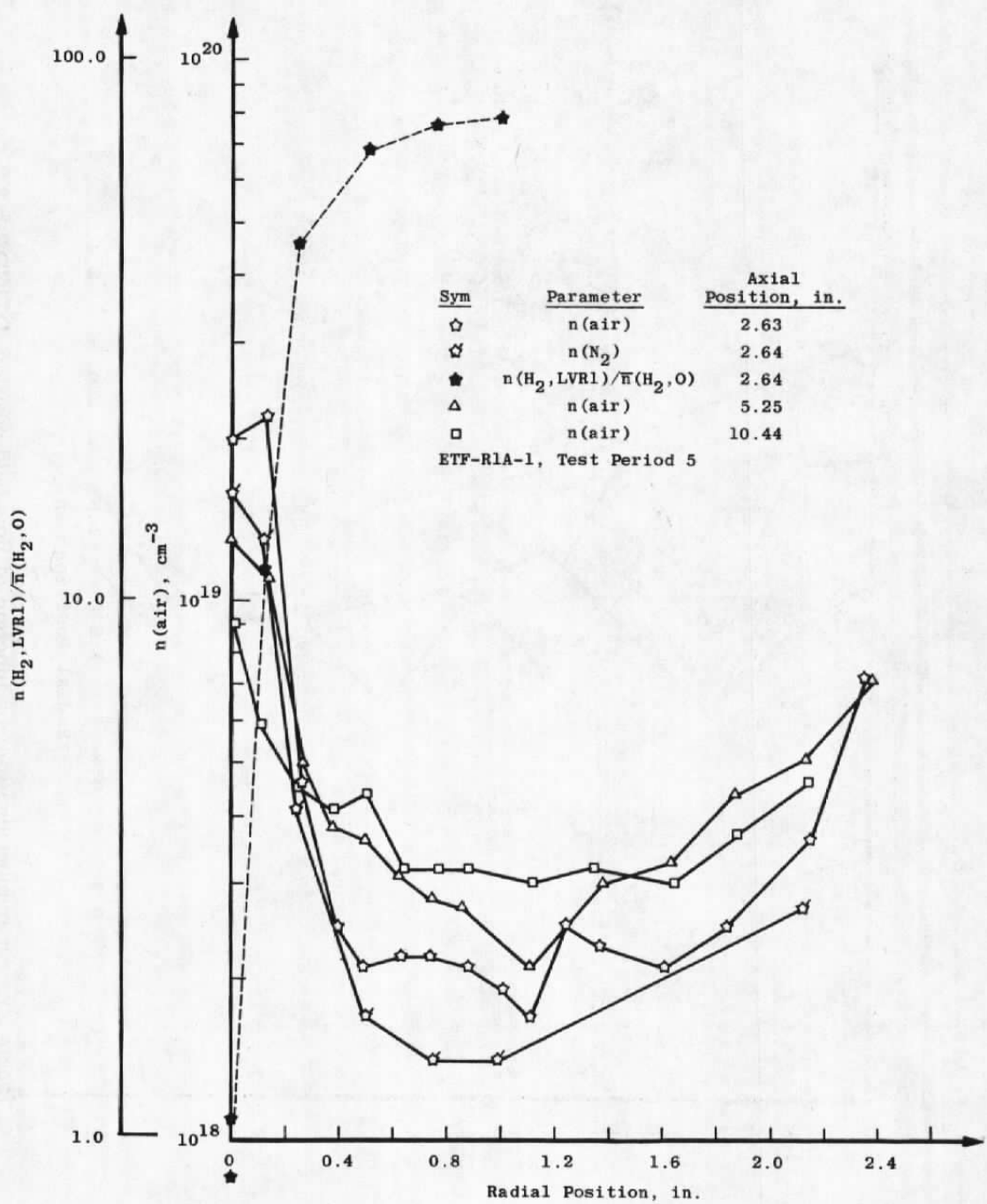


Figure 22. Number density as a function of flow-field position, DTINDR = 2.

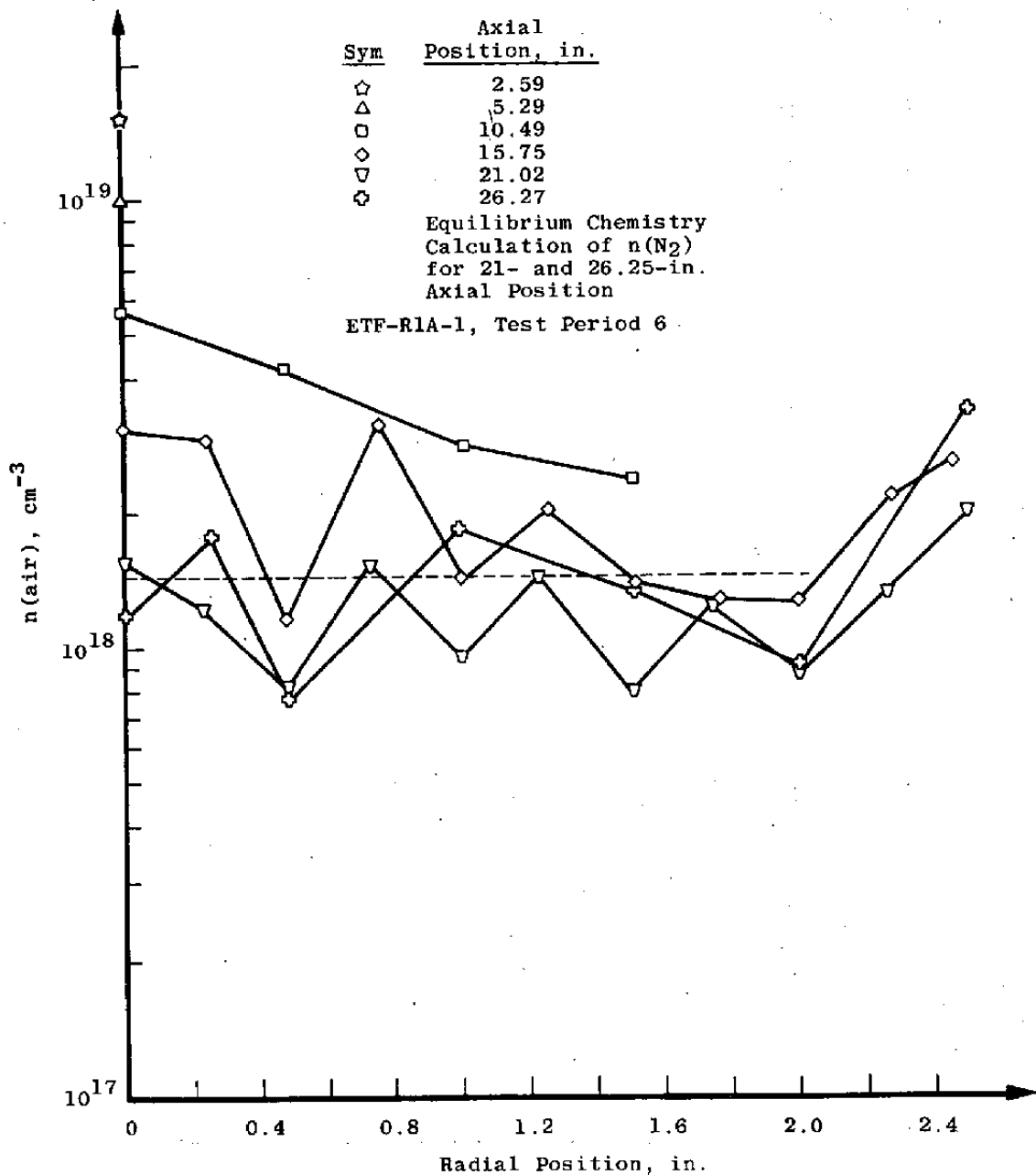


Figure 23. Number density as a function of flow-field position,
DTINDR = 10.

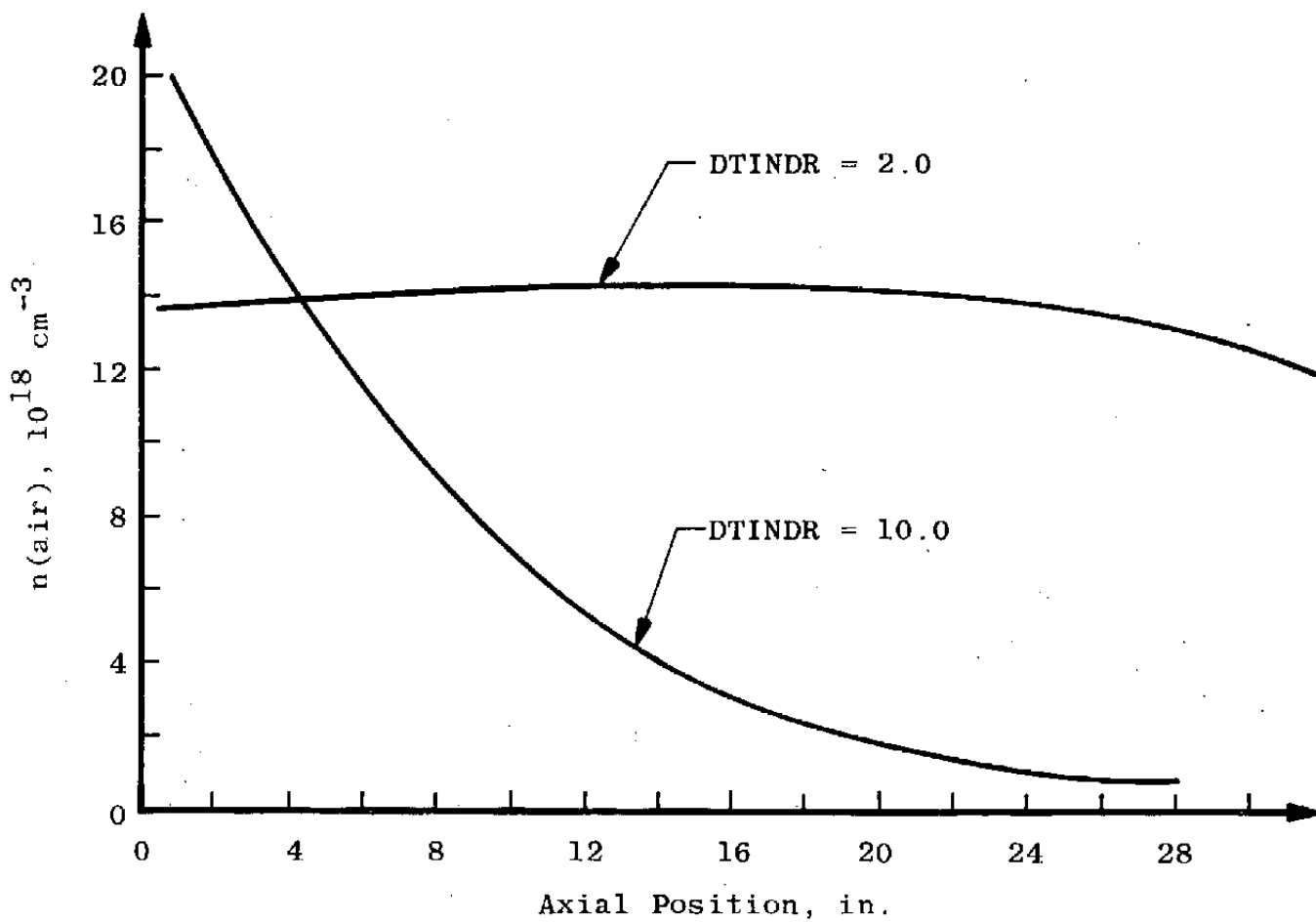


Figure 24. Axial centerline variation of $n(\text{air})$ for both test configurations.

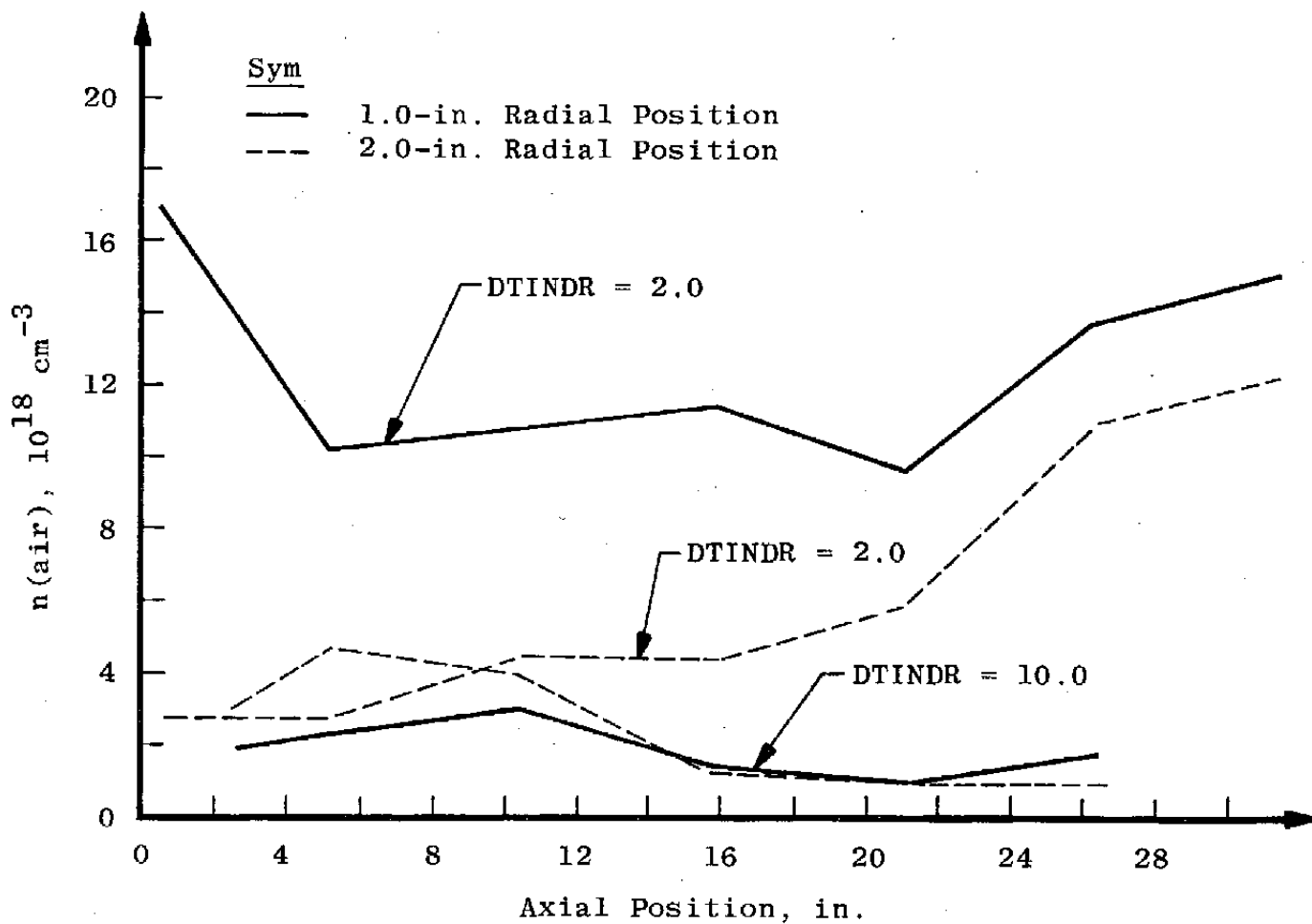


Figure 25. Axial variation of $n(\text{air})$ for both test configurations.

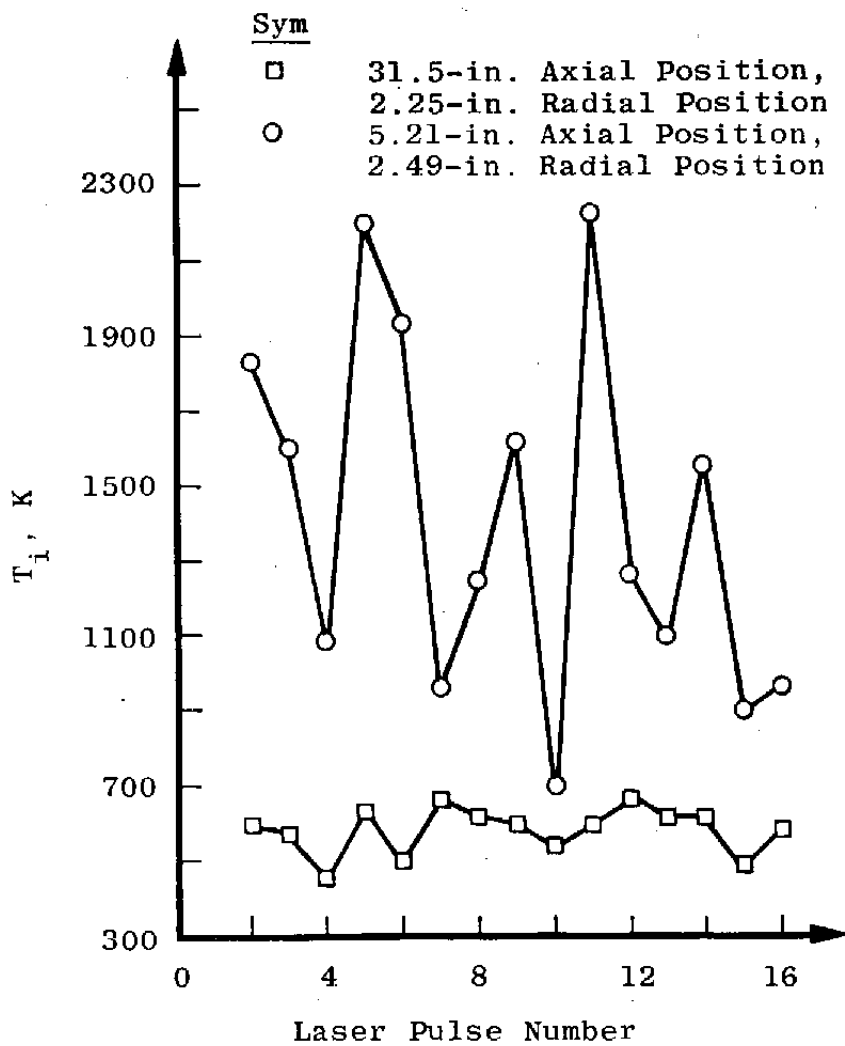


Figure 26. Instantaneous temperatures versus laser pulse number.

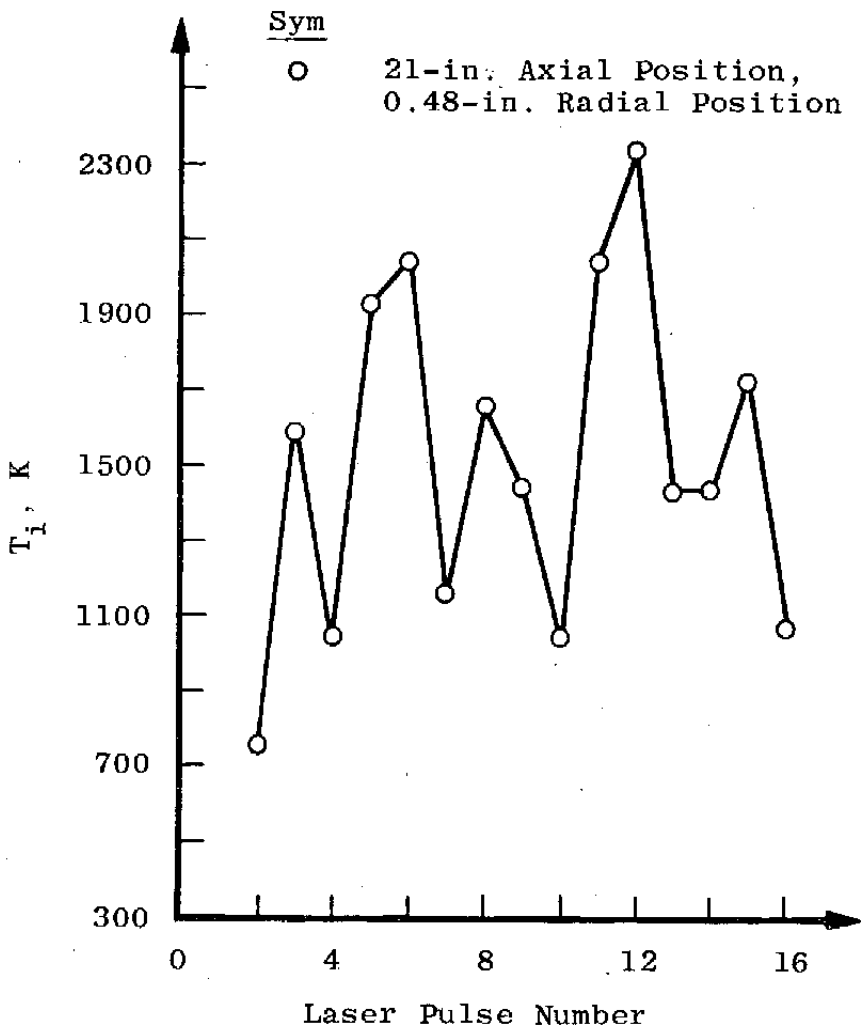


Figure 27. Instantaneous temperatures versus laser pulse number.

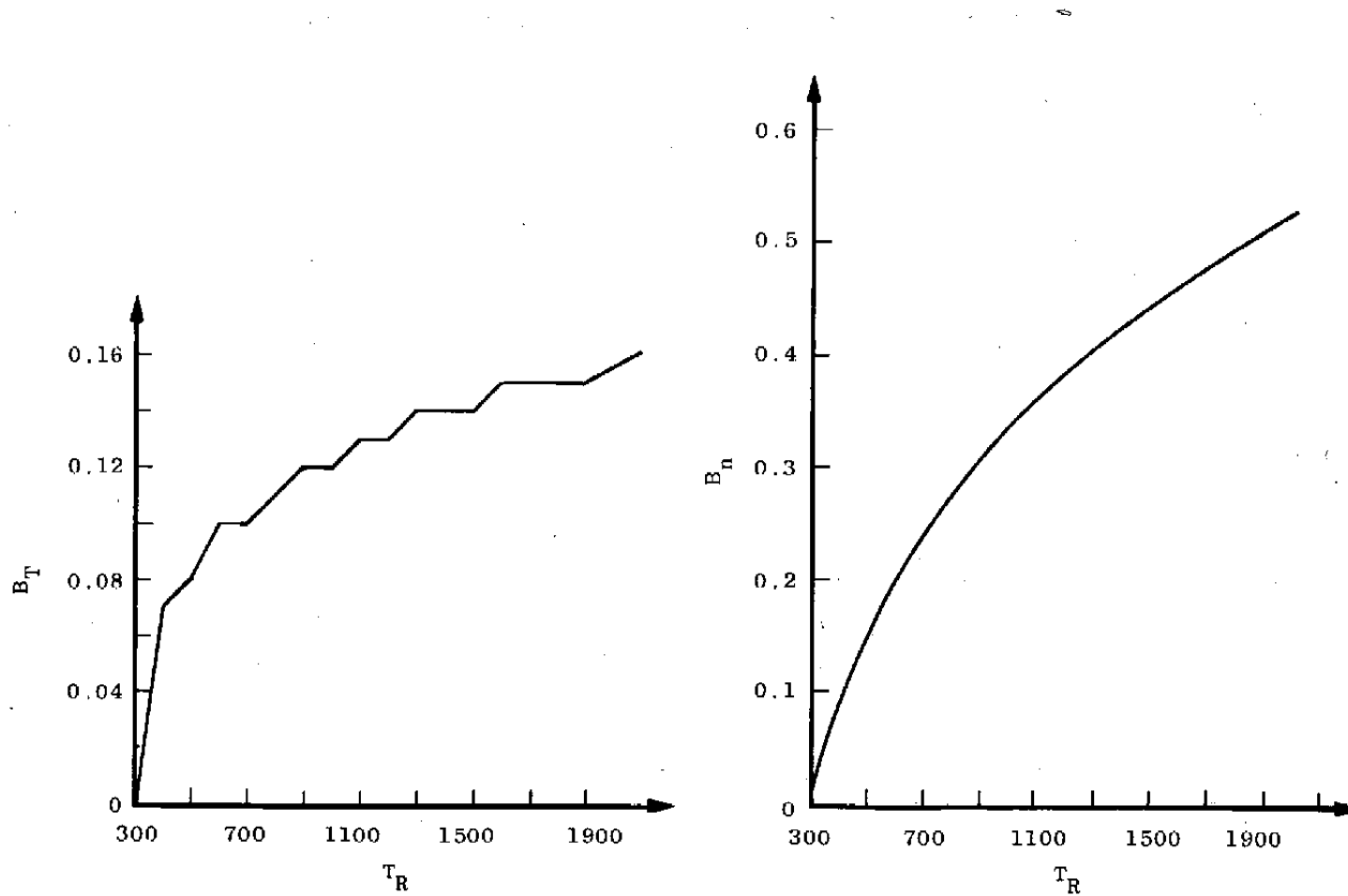


Figure 28. Systematic fractional error in temperature and number density measurements as a function of temperature.

Table 1. Measured Values of Temperature and Number Density and Estimated Uncertainty, DTINDR = 2

Test Period/ Data Point	Axial Position, in.	Radial Position, in.	$\bar{T}_R(R)$, K	S_T	\bar{T}_R , K	U_T	$\bar{n}(\text{air})$, cm^{-3}	S_n	U_n
4/ 1	31.5	0.05	495	0.037	501	0.043, 0.117	1.2×10^{19}	0.027	-0.126, -0.180
4/ 2		0.15	499	0.031	503	0.049, 0.111	1.4×10^{19}	0.020	-0.133, -0.173
4/ 3		0.23	523	0.037	531	0.049, 0.123	1.4×10^{19}	0.026	-0.141, -0.193
4/ 4		0.36	529	0.023	532	0.063, 0.109	1.4×10^{19}	0.017	-0.150, -0.184
4/ 6		0.51	534	0.023	537	0.064, 0.110	1.2×10^{19}	0.024	-0.146, -0.194
4/ 7		0.62	529	0.030	534	0.056, 0.116	1.2×10^{19}	0.024	-0.143, -0.191
4/ 8		0.73	536	0.025	539	0.063, 0.113	1.4×10^{19}	0.030	-0.141, -0.201
4/ 9		1.03	531	0.029	536	0.058, 0.116	1.5×10^{19}	0.019	-0.148, -0.186
4/10		1.25	486	0.034	491	0.045, 0.113	1.2×10^{19}	0.033	-0.112, -0.178
4/11		1.50	517	0.033	525	0.052, 0.118	1.2×10^{19}	0.023	-0.142, -0.188
4/12		1.75	556	0.026	600	0.074, 0.126	1.2×10^{19}	0.023	-0.127, -0.173
4/13		1.99	510	0.025	513	0.057, 0.107	1.2×10^{19}	0.019	-0.138, -0.176
4/14		2.25	583	0.027	587	0.068, 0.115	1.2×10^{19}	0.028	-0.167, -0.223
4/15	10.52	0	338	0.040	340	-0.012, 0.068	1.4×10^{19}	0.024	-0.026, -0.074
4/16	10.52	1.72	798	0.082	798	0.028, 0.192	4.5×10^{18}	0.101	-0.174, -0.376
4/21	10.53	0.36	371	0.109	409	-0.038, 0.180	1.6×10^{19}	0.087	-0.013, -0.187
4/22		1.71	912	0.076	924	0.044, 0.196	6.1×10^{18}	0.097	-0.215, -0.409
4/23		1.85	769	0.074	770	0.033, 0.181	5.6×10^{18}	0.104	-0.161, -0.369
4/24		1.96	977	0.051	986	0.069, 0.171	4.7×10^{18}	0.027	-0.303, -0.357
4/25		2.10	762	0.073	763	0.033, 0.179	3.9×10^{18}	0.038	-0.224, -0.300
4/26		2.25	1047	0.032	1048	0.093, 0.157	4.2×10^{18}	0.057	-0.290, -0.404
4/27		2.35	1058	0.052	1038	0.072, 0.176	3.1×10^{18}	0.090	-0.255, -0.435
4/28		2.46	1099	0.076	1059	0.050, 0.202	3.9×10^{18}	0.115	-0.235, -0.465
4/29		-0.01	323	0.014	323	-0.002, 0.026	1.4×10^{19}	0.051	-0.021, -0.086
4/30		0.42	329	0.014	329	0.008, 0.036	1.5×10^{19}	0.024	-0.017, -0.065
4/31		0.78	333	0.019	333	0.001, 0.039	1.5×10^{19}	0.041	-0.001, -0.083
4/32		1.18	561	0.093	598	0.007, 0.193	8.4×10^{18}	0.052	-0.148, -0.252
4/33		1.44	649	0.078	669	0.022, 0.178	6.7×10^{18}	0.076	-0.154, -0.306

Table 1. Continued

Test Period/ Data Point	Axial Position, in.	Radial Position, in.	$\bar{T}_R(R)$, K	$S_{\bar{T}}$	\bar{T}_R , K	U_T	$\bar{n}(\text{air})$, cm^{-3}	S_n	U_n
4/34	5.21	-0.05	317	0.008	317	0.002, 0.018	1.4×10^{19}	0.029	-0.001, -0.059
4/35		0.26	323	0.013	323	0.003, 0.023	1.4×10^{19}	0.049	0.015, -0.083
4/36		0.48	317	0.006	317	0.004, 0.016	1.1×10^{19}	0.023	-0.007, -0.053
4/37		0.72	322	0.021	322	-0.011, 0.031	1.1×10^{19}	0.039	0.005, -0.073
4/38		1.00	369	0.073	385	-0.013, 0.133	1.0×10^{19}	0.067	-0.015, -0.149
4/39		1.26	390	0.082	413	-0.010, 0.154	5.7×10^{18}	0.078	0.022, -0.178
4/40		1.50	678	0.095	696	0.005, 0.195	4.1×10^{18}	0.093	-0.147, -0.333
4/41		1.66	943	0.093	965	0.027, 0.213	1.8×10^{18}	0.104	-0.192, -0.400
4/42		1.78	920	0.082	935	0.038, 0.202	4.0×10^{18}	0.120	-0.165, -0.405
4/43		1.89	1126	0.102	1100	0.028, 0.232	2.4×10^{18}	0.163	-0.218, -0.544
4/44		2.01	1136	0.075	1118	0.055, 0.205	2.7×10^{18}	0.120	-0.244, -0.484
4/45		2.12	1285	0.067	1240	0.067, 0.201	1.5×10^{18}	0.088	-0.303, -0.479
4/46		2.21	1026	0.045	1031	0.078, 0.168	2.0×10^{18}	0.097	-0.245, -0.439
4/47		2.33	1208	0.082	1183	0.048, 0.212	1.2×10^{18}	0.100	-0.278, -0.478
4/48		2.49	1411	0.085	1362	0.055, 0.225	1.3×10^{18}	0.066	-0.349, -0.481
4/49	0.55	-0.06	319	0.008	319	0.005, 0.021	1.3×10^{19}	0.044	-0.006, -0.094
4/50		0.50	332	0.015	332	0.007, 0.037	1.6×10^{19}	0.032	-0.023, -0.087
4/51		1.02	328	0.018	328	0.004, 0.040	1.7×10^{19}	0.043	0.005, -0.081
4/52		1.25	346	0.019	346	0.011, 0.049	1.6×10^{19}	0.052	-0.002, -0.106
4/53		1.50	527	0.052	544	0.036, 0.14	8.3×10^{18}	0.062	-0.211, -0.335
4/54		1.66	631	0.044	638	0.056, 0.144	7.0×10^{18}	0.060	-0.156, -0.276
4/55		1.74	779	0.082	779	0.026, 0.190	3.1×10^{18}	0.097	-0.173, -0.367
4/56		1.86	715	0.046	718	0.056, 0.148	5.1×10^{18}	0.092	-0.156, -0.340
4/57		1.99	873	0.070	877	0.046, 0.186	2.6×10^{18}	0.076	-0.223, -0.375
4/58		2.13	796	0.097	796	0.012, 0.206	4.8×10^{18}	0.116	-0.159, -0.391
4/59		2.28	807	0.052	807	0.059, 0.163	3.2×10^{18}	0.080	-0.197, -0.357
4/60		2.36	648	0.050	657	0.050, 0.150	5.9×10^{18}	0.088	-0.137, -0.313
4/61		2.49	709	0.056	713	0.045, 0.157	3.4×10^{18}	0.085	-0.161, -0.331

Table 1. Concluded

Test Period/ Data Point	Axial Position, in.	Radial Position, in.	\bar{T}_R , K	$S_{\bar{T}}$	\bar{T}_R , K	U_T	\bar{n} (air), cm ⁻³	S_n	U_n
4/62	15.78	0.0	348	0.046	348	-0.011, 0.081	1.4×10^{19}	0.077	0.022, -0.132
4/63		0.27	331	0.017	331	0.005, 0.039	1.9×10^{19}	0.032	-0.005, -0.069
4/64		0.51	321	0.018	321	-0.005, 0.031	1.1×10^{19}	0.043	0.015, -0.071
4/65		0.77	404	0.099	408	-0.027, 0.171	1.4×10^{19}	0.092	-0.006, -0.190
4/66		1.01	414	0.101	418	-0.029, 0.173	1.1×10^{19}	0.084	-0.019, -0.187
4/67		1.23	552	0.083	590	0.015, 0.181	9.4×10^{18}	0.080	-0.115, -0.275
4/68		1.47	748	0.068	750	0.037, 0.173	5.9×10^{18}	0.115	-0.142, -0.372
4/69		1.72	611	0.067	631	0.033, 0.167	8.0×10^{18}	0.061	-0.153, -0.275
4/70		2.01	831	0.079	832	0.034, 0.192	4.2×10^{18}	0.078	-0.206, -0.362
4/71		2.23	841	0.061	842	0.053, 0.175	5.7×10^{18}	0.076	-0.212, -0.364
4/72		2.53	858	0.057	860	0.059, 0.173	3.6×10^{18}	0.059	-0.234, -0.352
4/73	21.07	-0.04	350	0.063	360	-0.021, 0.105	1.5×10^{19}	0.071	-0.017, -0.159
4/74		0.49	380	0.072	396	-0.004, 0.140	1.3×10^{19}	0.071	-0.017, -0.159
4/75		1.01	533	0.120	586	-0.023, 0.217	9.5×10^{18}	0.051	-0.092, -0.194
4/76		1.24	493	0.101	528	-0.015, 0.187	1.1×10^{19}	0.068	-0.098, -0.234
4/77		1.48	610	0.050	621	0.050, 0.150	7.9×10^{18}	0.059	-0.151, -0.269
4/78		1.77	607	0.051	618	0.049, 0.151	9.9×10^{18}	0.049	-0.159, -0.257
4/79		1.99	723	0.048	725	0.054, 0.150	5.8×10^{18}	0.049	-0.203, -0.301
4/80		2.27	687	0.036	690	0.064, 0.136	7.5×10^{18}	0.029	-0.208, -0.266
4/81		2.47	716	0.043	718	0.059, 0.145	5.8×10^{18}	0.052	-0.196, -0.300
4/82	26.24	0.01	449	0.050	461	0.026, 0.126	1.3×10^{19}	0.046	-0.084, -0.176
4/83		0.49	469	0.059	486	0.020, 0.138	1.2×10^{19}	0.066	-0.078, -0.210
4/84		0.98	508	0.051	522	0.033, 0.135	1.4×10^{19}	0.031	-0.133, -0.195
4/85		1.52	527	0.044	537	0.044, 0.132	1.3×10^{19}	0.071	-0.099, -0.241
4/86		2.00	570	0.040	578	0.056, 0.136	1.1×10^{19}	0.038	-0.152, -0.228
4/87		2.51	543	0.044	555	0.044, 0.132	9.2×10^{18}	0.048	-0.130, -0.226

Table 2. Measured Values of Temperature and Number Density and Estimated Uncertainty, DTINDR = 10

Test Period/ Data Point	Axial Position, in.	Radial Position, in.	$\bar{T}_R(R)$, K	$S_{\bar{T}}$	\bar{T}_R , K	U_T	$\bar{n}(\text{air})$, cm^{-3}	$S_{\bar{n}}$	U_n
6/ 1 & 2	15.75	0.0	855	0.070	862	0.046, 0.186	3.0×10^{18}	0.036	-0.33, -0.26
6/3		0.25	992	0.087	1016	0.039, 0.213	2.9×10^{18}	0.093	-0.44, -0.26
6/4		0.48	1033	0.095	1048	0.020, 0.220	1.1×10^{18}	0.121	-0.226, -0.468
6/5		0.76	918	0.059	926	0.061, 0.179	3.1×10^{18}	0.066	-0.247, -0.379
6/6		1.01	930	0.052	936	0.068, 0.172	1.4×10^{18}	0.104	-0.212, -0.420
6/7		1.26	1008	0.045	1014	0.076, 0.166	2.0×10^{18}	0.070	-0.268, -0.408
6/8		1.52	1145	0.035	1110	0.095, 0.165	1.4×10^{18}	0.054	-0.308, -0.415
6/9		1.77	1028	0.050	1033	0.074, 0.174	1.3×10^{18}	0.045	-0.297, -0.387
6/10		2.00	1043	0.039	1044	0.086, 0.164	1.3×10^{18}	0.040	-0.305, -0.385
6/11		2.24	1026	0.076	1027	0.056, 0.198	2.1×10^{18}	0.051	-0.291, -0.393
6/12		2.48	789	0.049	789	0.060, 0.158	2.6×10^{18}	0.067	-0.206, -0.340
6/13	21.02	0.0	1172	0.058	1077	0.069, 0.185	1.6×10^{18}	0.076	-0.279, -0.431
6/14		0.23	1335	0.073	1301	0.067, 0.213	1.2×10^{18}	0.106	-0.298, -0.510
6/15		0.48	1512	0.075	1466	0.045, 0.215	8.2×10^{17}	0.065	-0.371, -0.501
6/16		0.73	1332	0.078	1313	0.062, 0.218	1.5×10^{18}	0.045	-0.361, -0.451
6/17		1.00	1230	0.069	1214	0.062, 0.200	9.5×10^{17}	0.149	-0.237, -0.535
6/18		1.23	1267	0.041	1259	0.095, 0.177	1.4×10^{18}	0.038	-0.357, -0.433

Table 2. Continued

Test Period/ Data Point	Axial Position, in.	Radial Position, in.	$\bar{T}_R(R)$, K	S_T	\bar{T}_R , K	U_T	$\bar{n}(\text{air})$, cm $^{-3}$	S_n	U_n
6/19	21.02	1.50	1203	0.040	1197	0.090, 0.170	8.0×10^{17}	0.092	-0.290, -0.474
6/20		1.74	1140	0.062	1073	0.065, 0.189	1.3×10^{18}	0.038	-0.316, -0.392
6/21		1.99	976	0.042	981	0.078, 0.162	8.7×10^{17}	0.062	-0.268, -0.342
6/22		2.26	1078	0.037	1073	0.090, 0.164	1.3×10^{18}	0.023	-0.329, -0.375
6/23	↓	2.50	738	0.053	740	0.051, 0.157	2.5×10^{18}	0.048	-0.207, -0.303
6/24	26.27	0.0	1362	0.044	1351	0.096, 0.184	1.2×10^{18}	0.061	-0.353, -0.475
6/25	↓	0.26	1421	0.041	1420	0.099, 0.181	1.8×10^{18}	0.070	-0.356, -0.496
6/26		0.49	1335	0.064	1315	0.076, 0.204	7.7×10^{17}	0.112	-0.294, -0.519
6/27		0.99	1403	0.047	1390	0.089, 0.191	1.8×10^{18}	0.040	-0.382, -0.462
6/28		1.51	1142	0.051	1094	0.078, 0.180	1.3×10^{18}	0.030	-0.328, -0.388
6/29		2.0	1060	0.055	1058	0.072, 0.182	9.1×10^{17}	0.047	-0.303, -0.397
6/30	↓	2.5	809	0.039	809	0.072, 0.150	3.3×10^{18}	0.058	-0.219, -0.335
6/31	2.59	0.0	397	0.040	401	0.030, 0.110	1.5×10^{19}	0.040	-0.052, -0.132
6/32	5.29	0.0	446	0.032	449	0.043, 0.107	1.0×10^{19}	0.044	-0.079, -0.167
6/33	10.49	0.0	599	0.070	598	0.039, 0.179	5.6×10^{18}	0.049	-0.151, -0.249
6/34	↓	0.48	901	0.062	907	0.058, 0.182	4.2×10^{18}	0.078	-0.227, -0.383
6/35		1.01	897	0.042	900	0.078, 0.162	2.8×10^{18}	0.057	-0.247, -0.361
6/26	↓	1.51	980	0.039	986	0.081, 0.159	2.3×10^{18}	0.037	-0.294, -0.368

Table 2. Continued

Test Period/ Data Point	Axial Position, in.	Radial Position, in.	$\bar{T}_R(R)$, K	$S_{\bar{T}}$	\bar{T}_R , K	U_T	$\bar{n}(\text{air})$, cm^{-3}	S_n	U_n
5/3	2.65	0.0	357	0.040	360	0.000, 0.080	2.0×10^{19}	0.044	-0.018, -0.106
5/4		0.13	310	0.036	312	-0.030, 0.042	2.2×10^{19}	0.056	0.051, -0.061
5/5		0.26	570	0.070	589	0.028, 0.168	4.6×10^{18}	0.039	-0.153, -0.236
5/6		0.39	657	0.136	698	-0.036, 0.236	2.5×10^{18}	0.067	0.039, -0.201
5/7	2.63	0.49	810	0.096	810	0.015, 0.207	2.1×10^{18}	0.066	-0.212, -0.344
5/8		0.63	1070	0.134	1044	-0.010, 0.258	2.2×10^{18}	0.081	-0.265, -0.427
5/9		0.74	1106	0.088	1050	0.036, 0.212	2.2×10^{18}	0.055	-0.292, -0.402
5/10		0.88	1060	0.049	1055	0.076, 0.174	2.1×10^{18}	0.071	-0.278, -0.420
5/11		1.01	1021	0.087	1052	0.037, 0.211	1.9×10^{18}	0.072	-0.276, -0.420
5/12		1.11	955	0.108	1009	0.013, 0.229	1.7×10^{18}	0.064	-0.273, -0.401
5/13		1.24	663	0.104	706	-0.004, 0.204	2.5×10^{18}	0.054	-0.191, -0.299
5/14		1.37	763	0.138	769	-0.033, 0.243	2.3×10^{18}	0.105	-0.162, -0.372
5/15		1.61	598	0.115	686	-0.015, 0.215	2.1×10^{18}	0.067	-0.170, -0.304
5/16		1.84	570	0.113	622	-0.015, 0.215	2.5×10^{18}	0.060	-0.150, -0.270
5/17		2.13	459	0.063	486	0.015, 0.141	3.6×10^{18}	0.052	-0.094, -0.198
5/18	2.62	2.35	488	0.061	503	0.019, 0.141	7.2×10^{18}	0.038	-0.112, -0.188
5/19	2.62	0.0	361	0.039	361	0.001, 0.079	2.1×10^{19}	0.015	-0.045, -0.075
5/20	5.25	0.0	375	0.068	387	-0.007, 0.129	1.3×10^{19}	0.047	-0.036, -0.130
5/21		0.14	395	0.060	405	0.010, 0.130	1.1×10^{19}	0.076	-0.017, -0.169
5/23		0.38	801	0.133	800	-0.023, 0.243	3.8×10^{18}	0.050	-0.225, -0.325
5/24		0.50	930	0.097	946	0.023, 0.217	3.6×10^{18}	0.067	-0.193, -0.327
5/25		0.62	810	0.107	810	0.004, 0.218	3.1×10^{18}	0.074	-0.206, -0.354

Table 2. Concluded

Test Period/ Data Point	Axial Position, in.	Radial Position, in.	$\overline{T}_R(R)$, K	S_T	\overline{T}_R , K	U_T	$\bar{n}(\text{air}),$ cm^{-3}	S_n	U_n
5/26	5.25	0.75	904	0.079	914	0.041, 0.199	2.8×10^{18}	0.060	-0.248, -0.368
5/27		0.86	950	0.067	960	0.053, 0.187	2.7×10^{18}	0.045	-0.217, -0.307
5/28		1.11	840	0.080	841	0.033, 0.193	2.1×10^{18}	0.078	-0.208, -0.364
5/29		1.38	689	0.083	709	0.018, 0.184	3.0×10^{18}	0.069	-0.175, -0.313
5/30		1.63	773	0.067	843	0.047, 0.181	3.3×10^{18}	0.041	-0.247, -0.329
5/31		1.87	693	0.087	715	0.016, 0.190	4.4×10^{18}	0.089	-0.158, -0.339
5/32		2.13	686	0.032	709	0.069, 0.133	5.1×10^{18}	0.055	-0.189, -0.299
5/33		2.38	640	0.027	662	0.073, 0.127	7.1×10^{18}	0.001	-0.226, -0.228
5/34		0.0	331	0.038	334	-0.017, 0.059	1.5×10^{19}	0.032	-0.015, -0.079
5/36	10.44	0.01	480	0.040	488	0.039, 0.119	9.1×10^{18}	0.065	-0.082, -0.212
5/37		0.11	520	0.064	552	0.025, 0.153	5.9×10^{18}	0.053	-0.124, -0.230
5/38		0.25	590	0.107	661	-0.007, 0.207	4.5×10^{18}	0.075	-0.152, -0.302
5/39		0.38	630	0.054	649	0.046, 0.154	4.1×10^{18}	0.058	-0.165, -0.281
5/40		0.50	640	0.049	654	0.051, 0.149	4.4×10^{18}	0.051	-0.178, -0.280
5/41		0.64	840	0.048	841	0.065, 0.161	3.2×10^{18}	0.054	-0.232, -0.340
5/42		0.77	940	0.053	951	0.067, 0.173	3.2×10^{18}	0.043	-0.279, -0.365
5/43	10.43	0.88	850	0.069	853	0.046, 0.184	3.2×10^{18}	0.029	-0.263, -0.321
5/44		1.12	920	0.044	927	0.076, 0.164	3.0×10^{18}	0.034	-0.279, -0.347
5/45		1.35	870	0.043	872	0.074, 0.160	3.2×10^{18}	0.028	-0.270, -0.326
5/46		1.64	750	0.032	750	0.073, 0.132	3.0×10^{18}	0.018	-0.243, -0.279
5/47		1.88	830	0.045	830	0.068, 0.158	3.7×10^{18}	0.020	-0.265, -0.305
5/48		2.14	840	0.033	840	0.081, 0.147	4.6×10^{18}	0.045	-0.241, -0.331
5/49		0.01	450	0.054	480	0.024, 0.132	1.2×10^{19}	0.047	-0.093, -0.187

NOMENCLATURE

B	Fractional systematic error
B_n, B_T	Fractional systematic error of number density and temperature measurements, respectively
$C_F(\text{air}), C_F(\text{H}_2), C_F(\text{N}_2)$	Calibration factors for air, H_2 , and N_2 density determination using rotational line intensities
$C_F(\text{N}_2, Q)$	Calibration factor for N_2 density determination using the N_2 vibration-rotation band Q-branch
$C_{F_1}(T), C_{F_2}(T)$	Relative temperature dependence of the intensity of the rotational lines at 7010 Å for air and pure N_2 , respectively
$C_{F_3}(T)$	Relative temperature dependence of the intensity of the $J=1$, H_2 rotational line
$C_{F_4}(T)$	Relative temperature dependence of the intensity of the N_2 vibration-rotation band Q-branch
C_{F_R}	Relative sensitivity of the two detection channels
DTINDR	Duct-to-inner-nozzle diameter ratio
F/A	Fuel-to-air mass ratio
$I(7010 \text{ \AA}), I(7061.2 \text{ \AA})$	Intensity of the rotational Raman lines at 7,010 Å and 7061.2 Å, respectively
$I(J=1, \text{H}_2), I(J=2, \text{H}_2)$	Intensity of the $J=1$ and $J=2$ H_2 rotational Raman lines, respectively
I_m	Intensity, measured
$I(\text{N}_2, Q)$	Intensity of the N_2 vibration-rotation band Q-band
I_m^t	Intensity, test conditions, measured
J	Rotational level quantum number
k	Number of laser pulses used per data point

M, M'	Fluctuation measures
$n(\text{air})$	Number density of air
$n(N_2)$	Number density of N_2
$n(H_2)$	Number density of H_2
Q	Q-branch
R, \bar{R}	Measured intensity ratio and average measured intensity ratio, respectively
$R(T_R)$	Calculated rotational line intensity ratio
R_0	Intensity ratio corresponding to $\bar{T}_R(\bar{R})$
S	Fractional random error
$S_{\bar{n}}$	Fractional random error of the average number density measurement
$S_{\bar{n}}'$	Fractional rms deviation of intensity values used to determine average number density
$S_{\bar{n}}''$	Fractional deviation of $C_{F_1}(\bar{T}_R)$ values resulting from imprecision of the \bar{T}_R determination
$S_{\bar{R}}$	Fractional rms deviation of the intensity ratios used to determine an average temperature
$S_{\bar{T}}$	Fractional random error of the average temperature measurement
\hat{S}_T	Fractional rms deviation of the temperature values used to determine an average temperature
T, T_R	Temperature and rotational temperature, respectively
$\bar{T}_R(\bar{R})$	Initial average temperature value
$\bar{\bar{T}}_R$	Final, corrected average temperature value

$U; U_T; U_N$	Total uncertainty; total uncertainty in temperature measurement; total uncertainty in number density measurement
X	Mole fraction of species X
$\delta I(7010 \text{ \AA})$	Measured intensity residuals
δR	Measured intensity ratio residuals
δT	Measured temperature residuals
ϵ_M	Correction term for obtaining final average temperature
ϵ_n	Correction term for obtaining final average number density

SUBSCRIPTS

a, b	Denotes the two detector channels
c	Indicates a calculated value
i	Indicates an instantaneous value
m	Indicates a measured value

SUPERSCRIPTS

$\bar{}$	Indicates an ensemble average of the quantity beneath the bar
o	Indicates the value of a parameter at atmospheric conditions
t	Indicates the value of a parameter at test conditions